Self-Torque in Ferromagnetic using ST-FMR and Harmonic Measurements

CNF Project Number: 111-80
Principal Investigator(s): Robert A. Buhrman
User(s): Qianbiao Liu

Affiliation(s): Applied and Engineering Physics, Cornell University
Primary Source(s) of Research Funding: Department of Defense; Intelligence Advanced Research Projects Activity
Contact: buhrman@cornell.edu, ql63@cornell.edu
Primary CNF Tools Used: ASML, JEOL 6300, Veeco AFM

Abstract:

Spin-orbit torque in heavy metal/ferromagnet heterostructures with broken spatial inversion symmetry provides an efficient mechanism for manipulating magnetization using a charge current. We report the presence of a spin torque in a single ferromagnetic. According to the fitting results of ST-FMR and Harmonic measurements, it is clear the spin orbit torque that should come from the SHE and anomalous spin orbit torque of FM induced σz with σy spin current. However, there still remains a main problem to further clarify about the original of non-equilibrium spin accumulation between bottom Cu/FM interface and top FM/Cu interface.

Summary of Research:

When a charge current passes through a ferromagnet (FM) due to the imbalance in electron density of states at the Fermi level and scattering asymmetry between spin-up and spin-down electrons, it becomes polarized, thereby generating a net spin current flowing in the charge current direction. In addition to longitudinal charge and spin currents, transverse charge and spin currents are also generated by the anomalous Hall effect (AHE), leading to charge and spin accumulation at the side surfaces or edges at steady state. So far, the study of AHE has mainly been focused on charge accumulation because it can be detected directly as a voltage signal, and very little attention has been devoted to the spin accumulation. Recently, several groups have attempted to exploit the AHE-induced spin accumulation and related spin torque (ST) for magnetization switching applications in FM/nonmagnet (NM)/FM trilayers which, compared to spin-orbit torque (SOT) generated by the spin Hall effect (SHE), offers the possibility of controlling the spin polarization direction by manipulating the magnetization direction of one of the FM layers. However, there still remains a main problem to further clarify about the original of non-equilibrium spin accumulation between bottom Cu/FM interface and top FM/Cu interface.

We fabricated a series of Hall bar devices. We will discuss the spin torque, and the H_{FL0} values of all samples are shown on Figure 1. We get similar results with the ST-FMR results. The field-like torque in Cu/Py/Cu is opposite with MgO/Py/MgO, and the Ir/Py/Ir fall in between Cu/Py/Cu and MgO/Py/MgO. The torque in Cu/CoFeB/Cu have the same signal with Cu/Py/Cu. And the torque efficiency increases with increasing the FM thickness. All of these results mean the σ_y from the bulk effect. The possible mechanism is bulk SHE or the anomalous spin orbit torque.

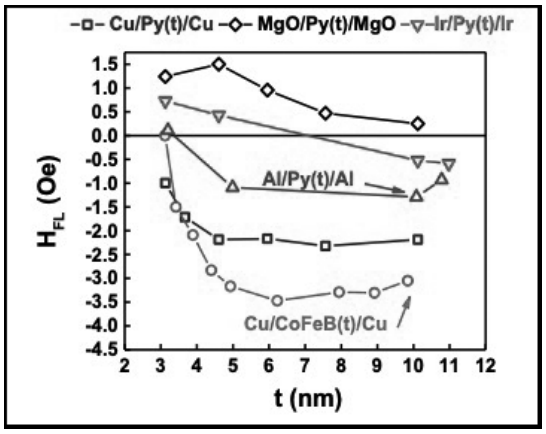

Figure 1: FM thickness dependence of H_{FL0}.

References:

[1] Z.Luo, Q.Zhang, Y.Xu, Y.Yang, X.Zhang and Y.Wu, Spin-Orbit Torque in a Single Ferromagnetic Layer Induced by Surface Spin Rotation. Phys. Rev. Appl. 11, 064021 (2019).

Spin Pumping and Non-Uniform Magnetic Excitation in Spin-Torque FMR Studies of the Spin Hall Effect

CNF Project Number: 111-80

Principal Investigator(s): Robert A. Buhrman

User(s): Ryan Tapping

Affiliation(s): Applied and Engineering Physics, Cornell University

Primary Source(s) of Research Funding: Cornell Center for Materials Research

Contact: buhrman@cornell.edu, rct76@cornell.edu

Primary CNF Tools Used: GCA 5x stepper, AJA sputtering tool

Abstract:

Spin-torque ferromagnetic resonance (ST-FMR) is a technique that was first used to show a surprisingly strong spin Hall effect (SHE) in certain heavy metals (HM) [1]. This method has since been widely deployed in the study of spin-orbit torques in HM/FM bilayers. However, recently it is unclear that ST-FMR always provides accurate, quantitative measures of the damping-like spin-torque efficiency ξ_{DL}, principally because of the unsettled role of spin-pumping and the inverse SHE in ST-FMR, but also because of the assumption that only the uniform mode is excited. Here we report on an extensive ST-FMR study of Pt/FM and HM/spacer/FM trilayers chosen such that the spin pumping effect is both strong and variable. We show that spin pumping, when significant, subtracts from the antidamping torque signal, resulting in $\xi_{FMR} < \xi_{DL}$. These results explain why ST-FMR often underestimates ξ_{DL} in comparison to quasi-static second harmonic results, the latter of which are generally confirmed by ST switching of MTJs.

Summary of Research:

Thin film samples were deposited onto 100 mm silicon wafers using our magnetron sputtering system. Structures were composed of, from bottom to top, Ta(1)/HM(t_{HM})/FM(t_{FM})/MgO(2)/Ta(1) with numbers in parenthesis representing the thickness of the layer in nanometers and t_{HM} and t_{FM} are the thicknesses of the heavy metal (HM) and ferromagnetic (FM) layers, respectively. Stacks were then patterned into 20 × 10 μm^2 microstrips using photolithography with the 5X g-line stepper at CNF and etched using our own ion milling system. The contacts were made using the AJA sputtering system at CNF. The schematic of our devices and measurement is shown in Figure 1.

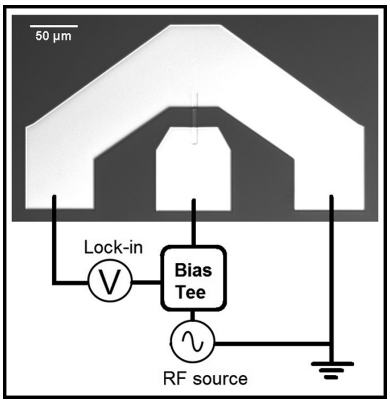

Figure 1: Microstrip with dimensions 20 × 10 μm^2 after fabrication and a schematic of the ST-FMR measurement.

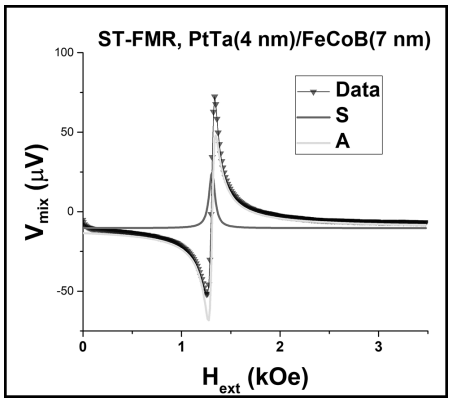

Figure 2: Example of voltage output from ST-FMR and a magnetic field sweep. The Lorentzian is fit with symmetric and antisymmetric components shown.

The spin torque efficiency (ξ) in these samples was determined using spin-torque ferromagnetic resonance (ST-FMR) [1,2]. A microwave frequency (RF) current is driven through the microstrip, which induces magnetic precession in the ferromagnetic layer via spin transfer torque. A magnetic field is swept at 45° to the microstrip and the voltage is measured by a lock-in amplifier. A lineshape analysis is done by fitting a Lorentzian function with symmetric (S) and antisymmetric (A) components as shown in Figure 2. The ratio of the prefactors S and A yield ξ_{FMR}.

Traditionally, spin pumping is not taken into account, and without the presence field-like torque ξ_{FMR} would be the same as the damping-like torque efficiency ξ_{DL}. Experimentally we achieve samples without a strong field-like torque by insertion of a Hf spacer layer between the HM and FM layers in the case of Pt based samples such as $Pt_{0.9}Ta_{0.1}$ [2]. However, when spin pumping is accounted for, the expression for ξ_{FMR} becomes more complicated as shown by the equation in Figure 3. Here we have separated two terms for the damping-like spin torque efficiency: one for the value obtained from the traditional analysis of the FMR signal, and one for the value obtained from the portion of the signal due to spin pumping. The entire portion of the signal subtracted from the FMR ξ_{DL} is due to spin pumping. Importantly, we can see some terms that would cause this signal to become larger such as higher HM resistivity samples and samples with thicker HM and FM layers.

We expected that the $Pt_{0.9}Ta_{0.1}$ alloy is a good HM for showing spin pumping because of its higher resistivity and large spin torque efficiencies as a Pt system. The result of an ST-FMR measurement of an 8 nm $Pt_{0.9}Ta_{0.1}$ sample with varying FeCoB thickness is shown in Figure 4. Here we see that the signal inferred from traditional FMR analysis is ξ_{DL} = 0.064. However, it is clear that ξ_{FMR} changes as a function of FM thickness. This is due to spin pumping and has the predicted behavior of subtracting from the signal and increasing in magnitude as the FM layer becomes thicker, as predicted in Figure 3. A quantitative analysis yields ξ_{DL} = 0.34 as measured from the spin pumping signal. This is much larger than the signal from traditional ST-FMR and agrees more closely with values obtained from similar Pt-based alloy systems [4] and with our own second harmonic measurements of $Pt_{0.9}Ta_{0.1}$ of around ξ_{DL} = 0.3 as well. Using different thicknesses of $Pt_{0.9}Ta_{0.1}$ we also observed spin pumping effects that were in relative strength to the thickness of the HM layer.

$$\xi_{\mathrm{FMR}} = \xi_{\mathrm{DL}}^{\mathrm{FMR}} - \frac{\xi_{\mathrm{DL}}^{\mathrm{SP}}\, e^{-\frac{t}{\lambda_{\mathrm{Hf}}}}}{\rho_{\mathrm{N}}} \frac{A}{(\Delta\rho/\rho)_{\mathrm{SMR}}} \left(B t_{\mathrm{F}} t_{\mathrm{N}} + \frac{\xi_{\mathrm{DL}}^{\mathrm{FMR}\,2}}{B t_{\mathrm{F}} t_{\mathrm{N}}} \right)$$

$$A = \frac{h}{e}\frac{\gamma\mu_0}{32\pi} \tanh\left(\frac{t_N}{2\lambda_N}\right) \frac{\sigma_{\mathrm{F}} t_{\mathrm{F}}}{\sigma_{\mathrm{N}} t_{\mathrm{N}} + \sigma_{\mathrm{F}} t_{\mathrm{F}}} \frac{1}{\alpha} \frac{\sqrt{H_{\mathrm{R}}(H_{\mathrm{R}} + 4\pi M_{\mathrm{eff}})}}{(H_{\mathrm{R}} + 2\pi M_{\mathrm{eff}})} \qquad B = \frac{\mu_0 e M_s}{\hbar} \sqrt{1 + \frac{4\pi M_{\mathrm{eff}}}{H_{\mathrm{R}}}}$$

Figure 3: The equation used for ST-FMR analysis with a spin pumping model.

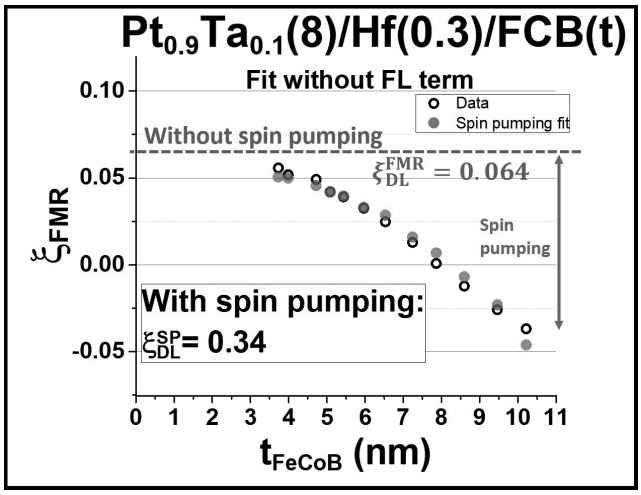

Figure 4: ST-FMR signal from an 8 nm $Pt_{0.9}Ta_{0.1}$ sample with Hf spacer and FeCoB. Fits to the data without the spin pumping model and with the spin pumping model are both shown.

Quantitative analysis yields results that agree well with other measurements, unlike the original analysis methods used which underestimate ξ_{DL}. We plan to do more experiments with different HM layers and also to fabricate more samples where we manipulate parameters such as the resistivity and also the spin torque signal itself with varying spacer layers. We expect to be able to model those results as well as those that also include a field-like torque term.

Conclusions and Future Steps:

We show that the spin pumping signal affects ST-FMR by subtracting from the signal and thus causing an underestimation of the damping-like spin torque efficiency of the HM layer if using only traditional analysis. In the $Pt_{0.9}Ta_{0.1}$ system, there is a clear suppression of the signal and it behaves in accordance with the equation in Figure 3.

References:

[1] Luqiao Liu, et al. Phys. Rev. Lett. 106, 036601 (2011).

[2] Chi-Feng Pai, et al. Phys. Rev. B. 92, 064426 (2015).

[3] Yongxi Ou, et al. Phys. Rev. B 94, 140414 (2016).

[4] L. Zhu, D.C. Ralph, and R.A. Buhrman, Phys. Rev. Applied 10, 031001 (2018).

Spin Torque Efficiency of Cobalt Iron Boron

CNF Project Number: 598-96

Principal Investigator(s): Daniel Ralph

User(s): Thow Min Cham

Affiliation(s): Laboratory for Atomic and Solid State Physics, Cornell University

Primary Source(s) of Research Funding: National Science Foundation/Division of Materials Research, Agency for Science Technology and Research (Singapore)

Contact: dcr14@cornell.edu, tc676@cornell.edu

Primary CNF Tools Used: Autostep i-line stepper, AJA sputter deposition, DISCO dicing saw

Abstract:

A spin polarized current is generated in a ferromagnet via the anomalous Hall effect (AHE) when an electric field is applied. The polarisation of the spins depend on the polarisation direction of the spin majority band, which can be controlled by applying an external magnetic field. Unlike spin currents generated in heavy metals where the spin polarisation is constrained by symmetry to be in plane, an out-of-plane component may be present. This enables high efficiency spin torque switching of magnets with perpendicular magneto-anisotropy. In this project, we investigate the charge to spin conversion efficiency of cobalt iron boron (CoFeB).

Summary of Research:

We quantify the spin torque efficiency of CoFeB by measuring the spin torque induced oscillation of a second CoFeB layer with perpendicular magnetic anisotropy, separated from the in-plane magnetised source layer by a titanium spacer layer. Similar work has been done using both CoFeB and permalloy spin source layers [1].

The CoFeB(4nm)/Ti(2nm)/CoFeB(1nm) heterostructures were first deposited by magnetron sputtering. Hall bars were then defined and etched out of the deposited thin film heterostructure using photolithography (Autostep i-line stepper) and ion-milling. Following this, a second level of photolithography was done and a second round of magnetron sputtering (AJA sputter deposition), to deposit titanium and platinum contact pads. A schematic of the heterostructure is shown in Figure 1. The fabricated devices were then measured on a projected field magnet probe station, where a sinusoidal voltage was applied across the hall bar and the transverse hall voltage whilst sweeping the external field strength and direction.

The longitudinal electric field generates a spin polarized current in the source layer, which flows in the transverse direction into the upper readout layer. As the spin polarized current travels into the ferromagnet, the local magnetization causes transverse components to dephase and transfer spin angular momentum in the process, applying a torque on the ferromagnet. This torque is also known as the anti-damping (AD) torque, and has the form $\tau \propto m \times (m \times \sigma)$. A second type of torque can also arise from the accumulation of spins at the interface between layers, and results in a field-like (FL) torque with the form $\tau \propto m \times \sigma$, where σ is the spin polarisation vector. This effective magnetic field due to these torques can be quantified using the Harmonic Hall method [2], where the ratio between the gradient of the second harmonic and the curvature of the first harmonic is proportional to the effective magnetic field.

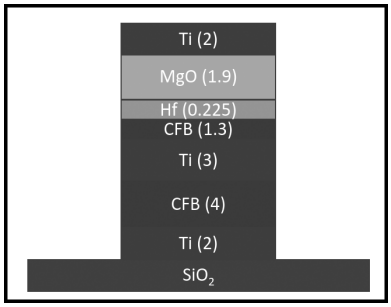

Figure 1: Schematic of the thin-film heterostructure deposited using magnetron sputtering. The two cobalt iron boron (CoFeB) layers are separated by a titanium spacer to minimise exchange coupling. A hafnium (Hf) dusting layer and a layer of magnesium oxide (MgO) was deposited on the top CoFeB layer to promote perpendicular magnetoanistropy (PMA) in the top magnet. Ti layers were used as capping layers below and on top of the heterostructure to prevent oxidation during the litho process.

To separate the AD torque from the FL torque, we apply an external magnetic field to tilt the out-of-plane magnetization of the readout magnet parallel and perpendicular to the current, such that only the AD torque and FL torques are non-zero respectively [3].

We compared the effective fields generated from the torques on the top magnetic layer with and without the bottom magnetic layer and found that there was a small but non-negligible effective field generated by the bottom CoFeB layer. Plots showing the variation of effective fields with the applied voltage are shown in Figures 2 and 3. Both the AD and FL torques increase with applied voltage and while the AD torque changes sign with mz, the FL torque remains the same sign, as expected from the formulae above.

Conclusion and Future Steps:

We have measured effective fields induced when a longitudinal current is applied through the ferromagnet CoFeB, supporting the theory that AHE in ferromagnets could lead to spin torque transfer via a spin polarized current. However, we have yet to confirm that this spin transfer torque does indeed have the same spin polarisation as the source magnet. This can be verified by sweeping the external field within the x-y plane and measuring the corresponding angular dependence of the spin torque driven oscillation of the upper readout magnet. In addition, other spin torque measurement techniques such as Spin torque ferromagnetic resonance, may be used to remove some of the thermal artifacts in the second harmonic measurement that may give an inaccurate effective field calculation.

References:

[1] Seung Heon C. Baek, Vivek P. Amin, Young Wan Oh, Gyungchoon Go, Seung Jae Lee, Geun Hee Lee, Kab Jin Kim, M.D. Stiles, Byong Guk Park, and Kyung Jin Lee. Spin currents and spin-orbit torques in ferromagnetic trilayers. Nature Materials, 17(6):509-513, June 2018.

[2] Masamitsu Hayashi, Junyeon Kim, Michihiko Yamanouchi, and Hideo Ohno. Quantitative characterization of the spin-orbit torque using harmonic Hall voltage measurements. Physical Review B-Condensed Matter and Materials Physics, 89(14), April 2014.

[3] Kevin Garello, Ioan Mihai Miron, Can Onur Avci, Frank Freimuth, Yuriy Mokrousov, Stefan Blugel, Stephane Auffret, Olivier Boulle, Gilles Gaudin, and Pietro Gambardella. Symmetry and magnitude of spin-orbit torques in ferromagnetic heterostructures. Nature Nanotechnology, 8(8):587-593, 2013.

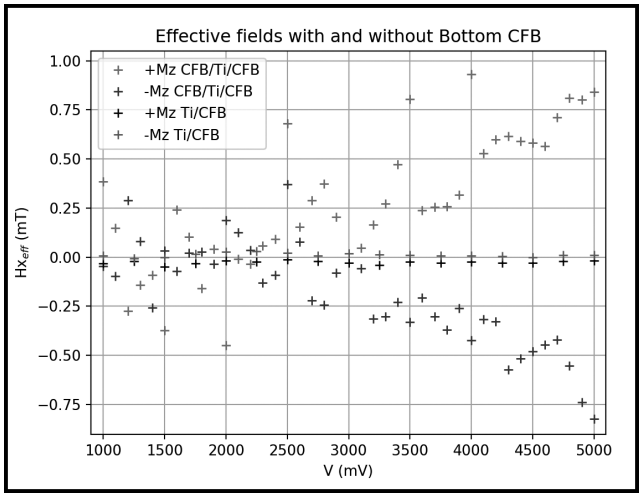

Figure 2: Anti-damping effective fields comparison with and without the CoFeB spin source layer. The effective field changes sign with the magnetization ofthe readout magnet (blue and red points), with both plots showing some voltage dependence, in contrast with the sample without the bottom CoFeB layer (black and green points). (See pages vi-vii for full color version.)

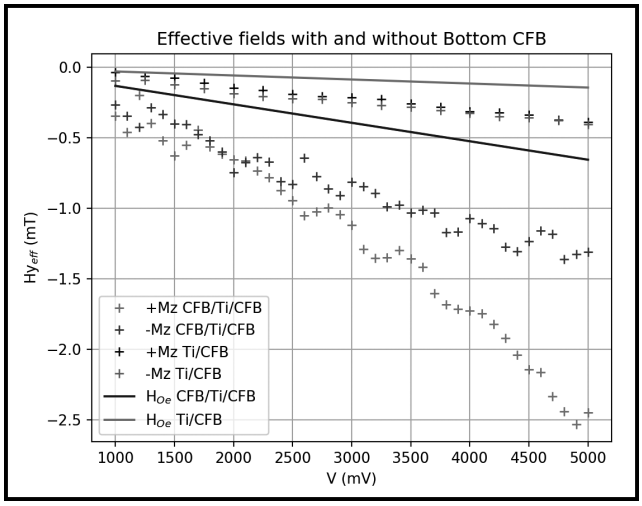

Figure 3: Field-like effective fields comparison with and without the CoFeB spin source layer. The effective field do not change sign with the magnetization of the readout magnet (blue and red points), with both plots showing some voltage dependence, in contrast with the sample without the bottom CoFeB layer (black and green points). The expected Oersted fields are plotted (blue and grey lines) to show that the measured effective fields are not solely a result of current induced Oersted fields. (See pages vi-vii for full color version.)

Microscopic Optically Powered Bubble Rockets

CNF Project Number: 900-00

Principal Investigator(s): Paul L. McEuen[1,2]

User(s): Samantha L. Norris[1], Michael F. Reynolds[1]

Affiliation(s): 1. Laboratory of Atomic and Solid State Physics, 2. Kavli Institute at Cornell for Nanoscale Science; Cornell University, Ithaca NY, USA

Primary Source(s) of Research Funding: Cornell Center for Materials Research with funding from the NSF MRSEC program (DMR-1719875), Air Force Office of Scientific Research (AFSOR) multidisciplinary research program of the university research initiative Grant FA2386-13-1-4118

Contact: plm23@cornell.edu, sn588@cornell.edu, mfr74@cornell.edu

Primary CNF Tools Used: Heidelberg DWL2000 mask writer, ABM contact aligner, Oxford 81/82/100/Cobra etchers, Xactix XeF_2 vapor etcher, AJA sputter deposition tool, Oxford PECVD, Arradiance ALD

Abstract:

We present artificial microswimmer devices that can be released from the substrate and propel themselves in fluid using bubble production and ejection. Unlike many other bubble-propelled microswimmers, ours operate in a range of fluids, including deionized water. These devices can be fabricated and released from the substrate in massive parallel using traditional photolithographic techniques. In this report, we discuss fabrication and characterization of these devices, and discuss initial results.

Summary of Research:

The ability to wirelessly power an artificial microswimmer lends itself well to a variety of applications, including *in vivo* cargo delivery [1]. Our technique for device fabrication and release from the substrate is fully scalable, allowing hundreds of thousands of devices to be studied simultaneously. In addition, the devices can be integrated with CMOS circuitry from commercial foundries, laying the foundation for additional complexity in the future.

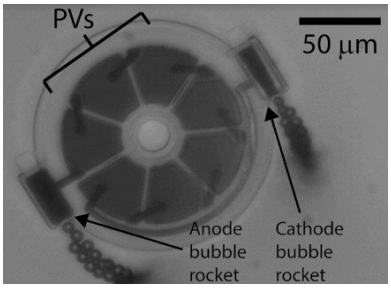

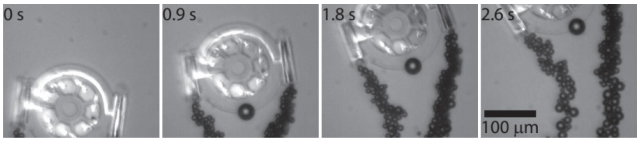

Figure 1, left: A bubble rocket in deionized water producing hydrogen at the cathode (left) and oxygen at the anode (right). Figure 2, above: A time lapse of a bubble rocket device swimming at an air-water interface, powered by a mercury lamp. The torque on the device is due to the inequality of hydrogen and oxygen production.

For bubble propulsion, we create devices consisting of silicon photodiodes that provide enough voltage to perform electrolysis at two protruding electrodes, producing hydrogen and oxygen gas at the cathode and anode respectively (Figure 1). Inspired by previous works on bubble rockets [2], the electrodes are tapered to eject the produced bubbles preferentially in one direction, causing the device to be propelled forward. Under an illumination intensity of about 100 nW/μm^2 at 532 nm, a 100 μm diameter device consisting of seven photodiodes can produce about 20 μA and 4.5V. A device using bubble ejection for self-propulsion in deionized water is depicted in Figure 2.

To create the silicon photodiode devices, we begin by selectively doping the top of the device layer with phosphosilicate glass to create a vertical PN junction. We then electrically isolate the photodiodes by dry etching to the buried oxide layer in the Oxford Cobra inductively coupled plasma (ICP) etcher. At this point, we also define the shape of our tapered electrodes in the silicon.

We then connect the photodiodes in series to each other and the electrodes, also conformally coating the silicon defining the electrodes in metal at this step. The metal electrodes and interconnects are platinum with a titanium adhesion layer deposited in the AJA sputter deposition tool. We encapsulate the photodiodes with silicon dioxide using the Oxford plasma enhanced chemical vapor deposition tool, leaving the metal electrodes protruding.

Finally, we connect aluminum supports to the devices and undercut the silicon underneath them with the Xactix XeF_2 etcher — this also etches the silicon of the rockets, leaving a hollow tapered oxide cylinder with a metal undercoating. Our devices can then be released from the substrate after immersion in any aluminum etchant.

Because the operation of these devices isn't dependent on a fuel source on the electrodes or in the solution, our bubble rockets operate in a range of solutions, even deionized water. The fabrication is entirely CMOS-compatible, allowing for the future integration with more complex circuitry to enable steering and phototaxis.

References:

[1] Gao, W., Dong, R., Thamphiwatana, S., Li, J., Gao, W., Zhang, L., and Wang, J. (2015). Artificial Micromotors in the Mouse's Stomach: A Step toward *in vivo* use of Synthetic Motors. ACS Nano.

[2] Gallino, G., Gallaire, F., Lauga, E., and Michelin, S. (2018). Physics of Bubble-Propelled Microrockets. Advanced Functional Materials.

Nanofabricated Superconducting Devices for Vortex Dynamics and Qubits

CNF Project Number: 1314-05

Principal Investigator(s): Britton L.T. Plourde

User(s): Kenneth Dodge, Jaseung Ku, Yebin Liu, Michael Senatore

Affiliation(s): Department of Physics, Syracuse University

Primary Source(s) of Research Funding: Army Research Office

Contact: bplourde@syr.edu, krdodgej@syr.edu, jku102@syr.edu, yliu166@syr.edu, masenato@syr.edu

Website: https://bplourde.expressions.syr.edu/

Primary CNF Tools Used: ASML Autostepper, JEOL 9500, Plasma-Therm 770

Abstract:

We fabricate superconducting microwave devices for studying the dynamics of vortices at low temperatures and for forming novel qubits. Vortices are quantized bundles of magnetic flux that thread many different superconductors over a particular range of applied magnetic field. By using disordered superconducting thin films to form high kinetic inductance wires combined with novel arrays of Josephson junctions, we are able to build structures that can lead to qubits that are protected against decoherence.

Summary of Research:

Superconducting microwave circuits play an important role in quantum information processing. Circuits composed of Josephson junctions and capacitors with superconducting electrodes can serve as qubits, the fundamental element of a quantum computing architecture. Various loss mechanisms limit the ultimate performance of these devices, including trapped magnetic flux vortices. Vortices can be trapped in the superconducting electrodes when background magnetic fields are present and contribute dissipation when driven with microwave currents [1]. Thus, techniques for controlling the trapping of vortices are critical to the development of large-scale quantum information processors with superconducting circuits. In addition, highly disordered superconducting films, including granular Al, can be used to form wires with a compact high kinetic inductance. When combined with novel arrays of Al-AlO_x-Al Josephson junctions, it is possible to implement new qubit designs that are protected against decoherence [2,3].

We fabricate our microwave resonators from various superconducting films, including aluminum, deposited onto silicon wafers in vacuum systems at Syracuse University. We define the patterns at CNF on the ASML stepper and transfer them into the films with a combination of reactive ion etching and liftoff processing. For defining Josephson junctions, we use the JEOL 9500 along with a dedicated deposition system at Syracuse University. We measure these circuits at temperatures of 100 mK and below in our lab at Syracuse University.

References:

[1] Song, C., Heitmann, T.W., DeFeo, M.P., Yu, K., McDermott, R., Neeley, M., Martinis, John M., Plourde, B.L.T.; "Microwave response of vortices in superconducting thin films of Re and Al"; Physical Review B 79, 174512 (2009).

[2] Doucot, B., Ioffe, L.; "Physical implementation of protected qubits"; Reports on Progress in Physics 75, 072001 (2012).

[3] Liu, Y., Dodge, K., Senatore, M., Zhu, S., Naveen, Shearrow, A., Schlenker, F., Klots, A., Faoro, L., Ioffe, L., McDermott, R., Plourde, B.; "Implementation of pi-periodic Josephson Elements for Topologically Protected Charge-Parity Qubits"; Bull. Am. Phys. Soc. 2019, http://meetings.aps.org/Meeting/MAR19/Session/S26.11.

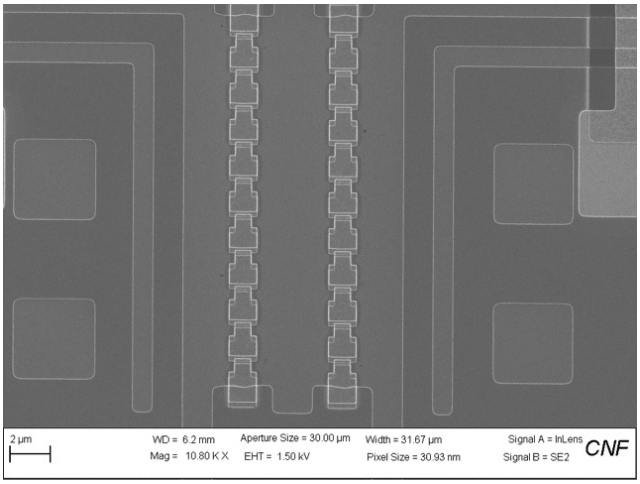

Figure 1: Scanning electron micrograph of inductors formed from arrays of Al-AlO_x-Al Josephson junctions for protected qubit design.

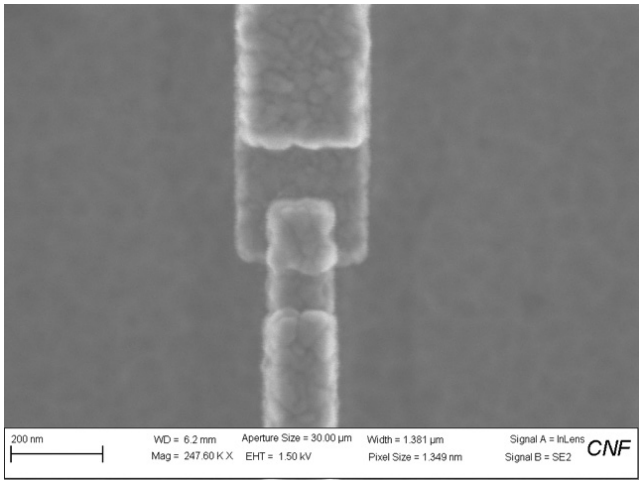

Figure 2: Scanning electron micrograph image of small-area Al-AlO_x-Al Josephson junction on protected qubit element.

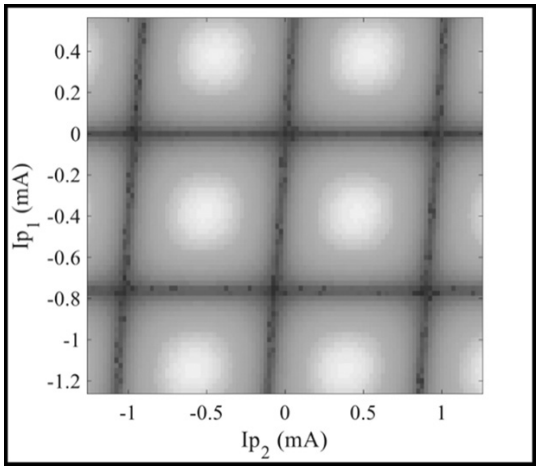

Figure 3: Two-dimensional flux bias current modulation of resonant frequency for readout microwave resonator coupled to qubit.

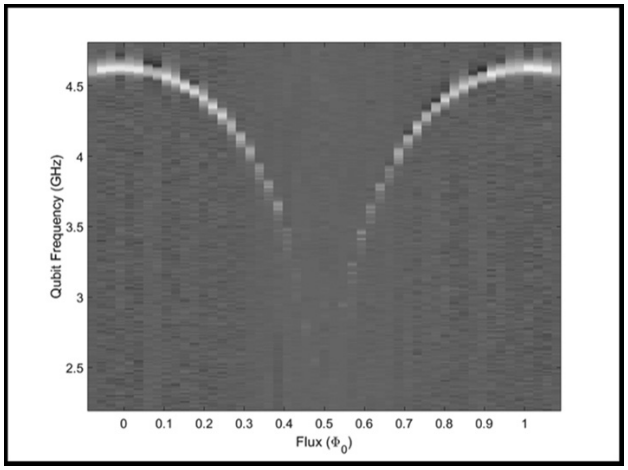

Figure 4: Flux modulation of qubit transition frequency.

Fabrication of Nanoscale Josephson Junctions for Quantum Coherent Superconducting Circuits

CNF Project Number: 1735-08

Principal Investigator(s): Britton L.T. Plourde

User(s): Andrew Ballard, Caleb Howington, Vito Iaia, Indrajeet

Affiliation(s): Department of Physics, Syracuse University

Primary Source(s) of Research Funding: Army Research Office, National Science Foundation

Contact: bplourde@syr.edu, alballar@syr.edu, cjhowing@syr.edu, vmiaia@syr.edu, indraje@syr.edu

Website: https://bplourde.expressions.syr.edu/

Primary CNF Tools Used: ASML Stepper, JEOL 9500, Plasma-Therm 770

Abstract:

We fabricate nanoscale superconductor tunnel junctions and other structures for experiments involving quantum coherent circuits. Such circuits have shown great promise in recent years for explorations of quantum mechanics at the scale of circuits on a chip and for forming qubits, the foundational elements of a quantum computer. The quantum state of these superconducting qubits can be manipulated with microwave radiation at low temperatures. In addition, we are developing alternative techniques for probing the state of these qubits and controlling their quantum state using superconducting digital circuitry, as well as superconducting metamaterial structures with novel microwave mode spectra for coupling to superconducting qubits.

Summary of Research:

The unique properties of nanoscale Josephson junctions enable a wide range of novel superconducting circuits for investigations in many diverse areas. In recent years, circuits composed of such junctions have emerged as promising candidates for the element of a quantum computer, due to the low intrinsic dissipation from the superconducting electrodes and the possibility of scaling to many such qubits on a chip [1]. The quantum coherent properties of the circuits are measured at temperatures below 50 mK with manipulation of the qubit state through microwave excitation.

We are currently working on a variety of experiments involving these nanoscale Josephson junctions and other superconducting structures that allow us to probe novel quantum effects in our microwave circuits. We are fabricating superconducting circuits for forming low-temperature detectors of single microwave photons and for implementing a new scheme for the efficient readout of the quantum state of superconducting qubits [2,3]. We are also working with collaborators at the University of Wisconsin, Madison to develop hybrid quantum/classical superconducting chips that allow us to perform coherent quantum control of a superconducting qubit based on digital pulses from a Single Flux Quantum (SFQ) circuit [4,5].

In another effort, we are using particular combinations of superconducting lumped-circuit elements to engineer metamaterial transmission lines that exhibit novel mode structures characteristic of left-handed materials. We are fabricating such metamaterial transmission lines from Al and Nb films on Si and characterizing these at low temperatures [6]. We are working on experiments to couple these left-handed lines to superconducting qubits for experiments involving the exchange of microwave photons [7].

We pattern these circuits at the CNF with nanoscale structures defined with electron-beam lithography on the JEOL 9500 integrated with photolithographically defined large-scale features. The junctions are fabricated using the standard double-angle shadow evaporation technique, in which a resist bilayer of copolymer and PMMA is used to produce a narrow PMMA airbridge suspended above the substrate. Evaporation of aluminum from two different angles with an oxidation step in between forms a small Al-AlO_x-Al tunnel junction from the deposition shadow of the airbridge. We have developed a process for defining these junctions with electron-beam lithography and we perform the aluminum evaporations in a dedicated chamber at Syracuse. We pattern large-scale features using the ASML stepper, with electron-beam evaporation of Al and sputter-deposition of Nb. Measurements of these circuits are performed in cryogenic systems at Syracuse University, including dilution refrigerators for achieving temperatures below 30 mK.

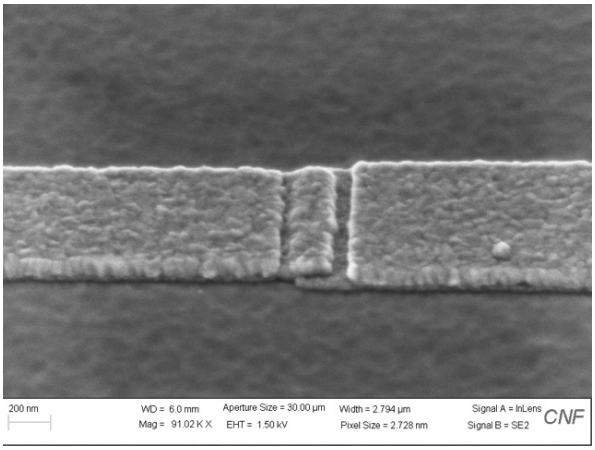

Figure 1: Scanning electron micrograph of Al-AlO_x-Al Josephson junction for superconducting qubit.

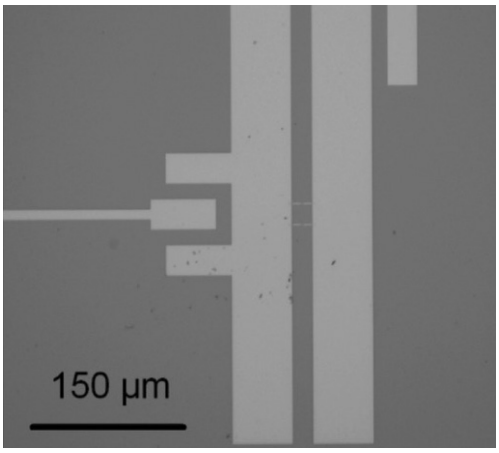

Figure 2: Optical micrograph of superconducting qubit coupled to metamaterial transmission line resonator.

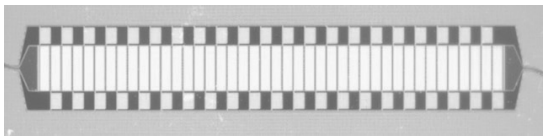

Figure 3: Optical micrograph of superconducting metamaterial transmission line resonator fabricated from Nb thin film on Si.

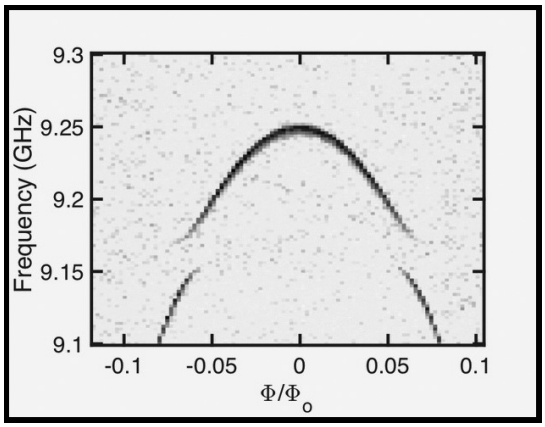

Figure 4: Spectroscopic measurement of flux modulation of qubit transition frequency for qubit coupled to metamaterial transmission line resonator.

References:

[1] Clarke, J. and Wilhelm, F.K.; "Superconducting quantum bits"; Nature, 453, 1031 (2008).

[2] Govia, L.C.G., Pritchett, Emily J., Xu, Canran, Plourde, B. L. T., Vavilov, Maxim G., Wilhelm, Frank K., McDermott, R.; "High-fidelity qubit measurement with a microwave-photon counter"; Physical Review A 90, 062307 (2014).

[3] Opremcak, A, Pechenezhskiy, I., Howington, C.,. Christensen, B.G., Beck, M.A., Leonard Jr, E., Suttle, J., Wilen, C., Nesterov, K.N., Ribeill, G.J., Thorbeck, T., Schlenker, F., Vavilov, M.G., Plourde, B.L.T., McDermott, R.; "Measurement of a Superconducting Qubit with a Microwave Photon Counter"; Science 361, 1239 (2018).

[4] McDermott, R., Vavilov, M.; "Accurate Qubit Control with Single Flux Quantum Pulses"; Physical Review Applied 2, 014007 (2014).

[5] Leonard, E., Beck, M., Nelson, JJ, Christensen, B., Thorbeck, T., Howington, C., Opremcak, A.,Pechenezhskiy, I., Dodge, K., Dupuis, N., Ku, J., Schlenker, F., Suttle, J. Wilen, C., Zhu, S., Vavilov, M., Plourde, B, McDermott, R.. "Digital coherent control of a superconducting qubit"; Phys.Rev.Applied 11, 014009 (2019).

[6] Wang, H., Zhuravel, A., Indrajeet, S., Taketani, B., Hutchings, M., Hao, Y., Rouxinol, F., Wilhelm,F., LaHaye, M.D., Ustinov, A., Plourde, B.; "Mode Structure in Superconducting Metamaterial Transmission Line Resonators"; Physical Review Applied 11, 054062 (2019).

[7] Indrajeet, S., Wang, H., Hutchings, M., LaHaye, M., Taketani, Bruno, Wilhelm, F., Plourde, B.; "Qubit Dynamics in a Multi-mode Environment with a Superconducting Metamaterial Resonator"; Bull. Am. Phys. Soc. 2019, http://meetings.aps.org/Meeting/MAR19/Session/P26.4.

Local Photothermal Control of Phase Transitions for On-Demand Room-Temperature Rewritable Magnetic Patterning

CNF Project Number: 2091-11

Principal Investigator(s): Gregory D. Fuchs[1], Darrell G. Schlom[2]

User(s): Isaiah Gray[1]

Affiliation(s): 1. School of Applied and Engineering Physics, 2. Materials Science and Engineering; Cornell University

Primary Source(s) of Research Funding: Cornell Center for Materials Research from the National Science Foundation MRSEC Program, Grant No. DMR-1719875

Contact: gdf9@cornell.edu, ig246@cornell.edu

Primary CNF Tools Used: GCA 5x stepper

Abstract:

The ability to make controlled patterns of magnetic structures within a nonmagnetic background provides the foundation of magnetic memory and logic devices, allows the creation of artificial spin-ice lattices, and enables the study of magnon propagation. Here, we report a novel approach for magnetic patterning that allows repeated creation and erasure of arbitrary shapes of thin-film ferromagnetic structures. This strategy is enabled by epitaxial $Fe_{0.52}Rh_{0.48}$ thin films designed so that both ferromagnetic and antiferromagnetic phases are stable at room temperature. Starting with the film in a uniform antiferromagnetic state, we demonstrate the ability to write arbitrary patterns of the ferromagnetic phase with submicron spatial resolution by local heating with a focused pulsed laser. The ferromagnetic patterns can be erased by cooling below room temperature and the material repeatedly re-patterned.

Summary of Research:

Local patterning of ferromagnetic regions forms the basis of magnetic logic and memory devices [1] as well as spin-wave devices such as magnon waveguides [2] and magnonic crystals [3]. Magnetic nanostructures are typically patterned with lithography and etching, which cannot be easily erased and repatterned. In this work [4] we present a platform for rewritable magnetic patterning, which is based on the 1st-order phase transition from antiferromagnet (AF) to ferromagnet (FM) in near 50/50 stoichiometric iron-rhodium (FeRh) [5].

Epitaxial FeRh films are grown on MgO(001) via molecular-beam epitaxy. Lower Rh concentration decreases the transition temperature T_C [6]; we therefore tune the stoichiometry to $Fe_{0.52}Rh_{0.48}$ during growth, which sets $T_C \approx 430$ K such that both AF and FM phases are stable at room temperature.

In Figure 1 we show radial plots of magnetization M as a function of magnetic field H (clockwise) and temperature T (radial). We plot $M(H,T)$ in both the cooling branch (Figure 1(a)) and the heating branch (1(b)) of the transition, which highlights the dissimilar T_C in heating (AF to FM) and cooling (FM to AF).

Plots of $M(T)$ and resistance $R(T)$ at constant field in Figure 1(c) and 1(d) show that both AF and FM phases are stable at 293 K.

Having established room-temperature phase bistability, we pattern local FM regions using a laser focused to ~ 650 nm spot size at 10.8 mJ/cm^2 fluence, which locally heats the FeRh by 90K. This temperature increase induces the FM phase, which remains after the laser is turned off. We image the resulting patterns with the same laser at low (0.6 mJ/cm^2) fluence, using anomalous Nernst microscopy [7].

In this technique, the focused laser generates a local thermal gradient ∇T, which induces an electric field $\boldsymbol{E}_{ANE}$ proportional to the moment: $\boldsymbol{E}_{ANE} = -N\mu_0 \nabla T \times \boldsymbol{M}$.

We raster scan the laser and measure the $\boldsymbol{E}_{ANE}$-induced voltage drop across the entire sample, which builds up a map of in-plane $\boldsymbol{M}$. By using low fluence, we image magnetic contrast without perturbing it.

Two examples of patterning and imaging are shown in Figure 2. In Figure 2(a) we show three anomalous Nernst effect (ANE) images at room temperature: one in the uniform AF phase before patterning, one after laser-writing FM patterns spelling out the authors' affiliation, and one after cooling the film below room temperature and warming back to room temperature. To subtract out artifacts from varying thermal conductivity and isolate the magnetic signal, each image presented is the

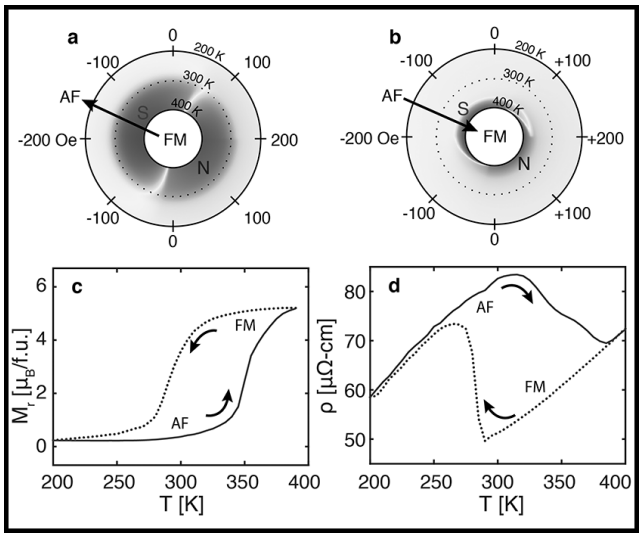

Figure 1: (a,b) Magnetization M *as a function of temperature* T *and magnetic field* H *in epitaxial* $Fe_{0.52}Rh_{0.48}$ *grown on MgO(001). The phase transition is observed in (a) the cooling branch and (b) the heating branch, showing the dissimilar transition temperatures between antiferromagnet to ferromagnet and vice versa. (c)* M*(*T*) and* R*(*T*) at fixed field show that both AF and FM phases are stable at room temperature.*

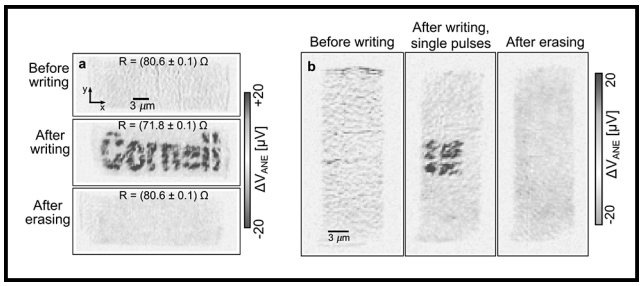

Figure 2: Laser-writing ferromagnetic regions within an antiferromagnetic background and imaging the written regions using anomalous Nernst microscopy. (a) Imaging at room temperature in the AF phase, after laser-writing, and after erasing by cooling and warming back to room temperature. (b) Demonstrating ultrafast patterning by imaging a 5 μm square written using a single 3 ps laser pulse per pixel. (See pages vi-vii for full color version.)

half-difference between raw ANE images acquired at 1 kOe magnetic field applied along opposite directions. Light red contrast represents uncompensated moments in the AF phase [8], while dark red represents FM moments. The images show that ferromagnetic regions can be patterned with submicron resolution, and that they are erased by cooling the sample below room temperature. Finally, in Figure 2(b) we demonstrate ultrafast magnetic patterning by writing a 5 × 5 μm square using a single 3 ps-wide laser pulse per pixel.

In summary, we demonstrate a platform for room-temperature rewritable magnetic patterning in bistable FeRh. Laser-written FM regions can be erased by cooling, and the film can be erased and rewritten many times with no measurable damage to the crystal structure. Our results could enable rapid prototyping of a variety of magnetic devices, including magnonic crystals and logic devices.

References:

[1] S. N. Piramanayagam, T. C. Chong, Developments in Data Storage: Materials Perspective, Wiley, 2011.

[2] A. V. Chumak, et al., Nat. Phys. 11, 453 (2015).

[3] B. Lenk, H. Ulrichs, F. Garbs, and M. Müzenberg, Phys. Rep. 507, 107-136 (2011).

[4] A. B. Mei*, I. Gray*, et al., Adv. Mater. (accepted), arXiv:1906.07239 (2019).

[5] J. B. McKinnon, D. Melville, and E. W. Lee, J. Phys. C 3, S46 (1970).

[6] A. B. Mei, et al., Appl. Phys. Lett. 113, 082403 (2018).

[7] J. M. Bartell*, D. H. Ngai*, et al., Nat. Comm. 6, 8460 (2015).

[8] I. Gray, et al., Phys. Rev. Mater. 3, 124407 (2019).

Topological Hall Effect in MnFeGe/FeGe Bilayer Thin Films

CNF Project Number: 2091-11
Principal Investigator(s): Gregory Fuchs
User(s): Varshith Kandula

Affiliation(s): Applied and Engineering Physics, Cornell University
Primary Source(s) of Research Funding: Cornell Center for Materials Research (DMR-1719875)
Contact: gdf9@cornell.edu, vk332@cornell.edu
Website: http://fuchs.research.engineering.cornell.edu/
Primary CNF Tools Used: GCA 5x stepper, AJA ion mill, SC4500 even-hour evaporator

Abstract:

We investigate the topological Hall effect (THE) in MnFeGe/FeGe and MnFeGe/FeGe/Pt thin films using Hall measurements. These materials host nanometer-sized quasiparticles called skyrmions in a range of temperature and magnetic field. Skyrmions are promising candidates for future applications in high density magnetic storage devices, for example, as bits to store information, and in racetrack type computing devices owing the low current densities required to move them. The presence of skyrmions results in an effective magnetic field acting on transport electrons that appears as an extra term to the Hall resistance. We compare the THE resistance of MnFeGe/FeGe and MnFeGe/FeGe/Pt and find that it is extended in the Pt-capped film.

Summary of Research:

MnFeGe and FeGe have a chiral B20 structure that induces antisymmetric exchange called the Dzyaloshinski-Moriya Interaction (DMI) that favors canting of magnetic spins. In conjunction with the Zeeman, exchange, magnetostatic, magnetocrystalline anisotropy and dipole-dipole interaction terms it stabilizes exotic spin structures called skyrmions [1] in a region of the temperature and external magnetic field. These quasiparticles are topologically stabilized once formed, and a finite energy is required to collapse a skyrmion into a trivial ferromagnetic (antiferromagnetic) state. A major direction of current research is stabilizing skyrmions at room temperature and zero magnetic fields in thin films for potential applications. Skyrmions can also be stabilized at ferromagnet (FM)/heavy metal (HM) interfaces [2] at room temperature due to interfacial DMI from large spin-orbit coupling (SOC) originating in the HM layer.

Skyrmions can be imaged directly by Lorentz transmission electron microscopy (LTEM), electron holography (EH), and magnetic force microscopy (MFM), and the skyrmion lattice can be detected in reciprocal space by small angle neutron scattering (SANS) and resonant elastic X-ray scattering (REXS) [3]. Indirect methods of detecting the skyrmion phase boundary include AC magnetic susceptibility (ACMS), microwave absorption spectroscopy (MAS), magnetoresistance vs. field and topological Hall effect measurements.

The presence of topologically non-trivial spin textures such as magnetic skyrmions can be modelled by an emergent magnetic field, which contributes an additional term to the Hall effect signal (the topological Hall resistance). The Hall resistance has three contributions; 1) an ordinary Hall resistance (OHR) due to the Lorentz force on electrons proportional to the external magnetic field, 2) an anomalous Hall resistance (AHR) in ferromagnets arising from SOC and/or spin dependent scattering that is approximately proportional to the magnetization, and 3) topological Hall resistance (THR). By subtracting the calculated OHR and AHR contributions from the measured Hall resistance the THR can be estimated in a sample.

Figure 1 shows the fabricated Hall device of two samples, MnFeGe(20nm)/FeGe(7nm) and MnFeGe(20nm)/FeGe(4nm)/Pt(1.5nm). The Heidelberg mask writer DWL2000 was used to make photomasks and photolithography was performed on a GCA 5x Stepper. An AJA ion mill was used to etch the material into a Hall geometry. An SC4500 even-hour evaporator was used to make gold contact pads for electrical measurements. Hall resistance as a function of the magnetic field at temperatures between 40 Kelvin (K) - 240 K was measured in a Quantum Design physical property measurement system (PPMS).

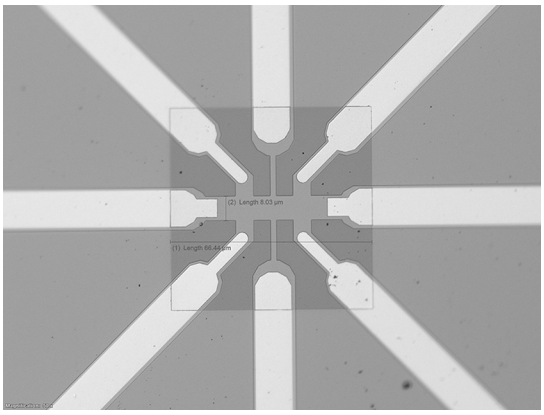

Figure 1: Patterned Hall bar device.

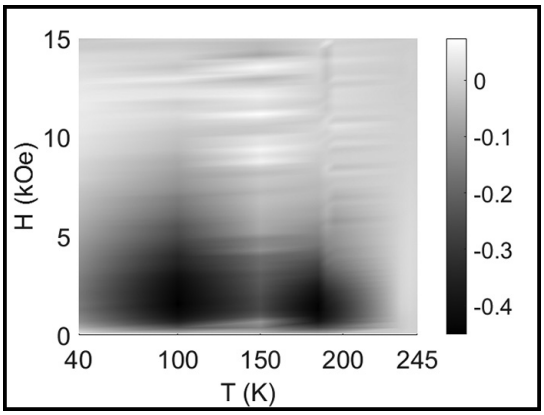

Figure 2: THR of MnFeGe(20nm)/FeGe(7nm).

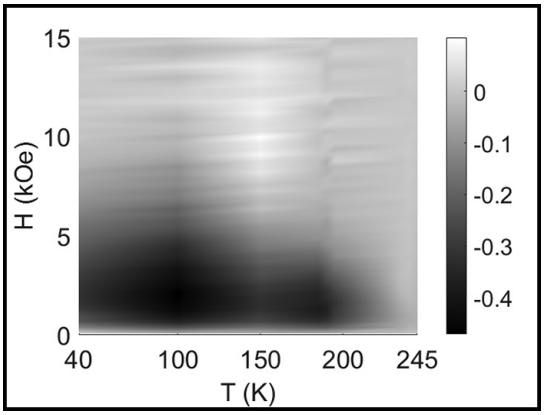

Figure 3: THR of MnFeGe(20nm)/FeGe (4nm)/Pt(1.5nm).

Figure 2 shows the THR (resistance given in ohms) as a function of temperature and external field for MnFeGe/FeGe and Figure 3 shows the THR for MnFeGe/FeGe/Pt. MnFeGe is known to host skyrmions below a critical temperature (T_c) ~ 180K and FeGe hosts skyrmions below T_c ~ 270K.

We observe a broadened phase space of the THR in the Pt-capped sample compared the MnFeGe/FeGe bilayer, which could be due to an increase in skyrmion stability from the interplay between interfacial DMI from Pt and bulk DMI from MnFeGe and FeGe. The THR could also arise due to other non-trivial magnetic textures and further experiments are needed to identify its origin.

Conclusions and Future Steps:

We have measured the THR of skyrmion-hosting B20 thin films and report a broadened phase space in the heavy metal capped sample. To further study the magnetic phases in our thin films we have fabricated spin-transfer ferromagnetic resonance (ST-FMR) [4] devices, which could shed light on resonant dynamics of the skyrmion phase.

References:

[1] Nagaosa, N., and Tokura, Y. (2013). Topological properties and dynamics of magnetic skyrmions. Nature Nanotechnology, 8(12), 899-911.

[2] Moreau-Luchaire, C., et al. (2016). Additive interfacial chiral interaction in multilayers for stabilization of small individual skyrmions at room temperature. Nature Nanotechnology, 11(5), 444-448.

[3] Mathur, N., Stolt, M. J., and Jin, S. (2019). Magnetic skyrmions in nanostructures of non-centrosymmetric materials. APL Materials, 7(12).

[4] Liu, L., Moriyama, T., Ralph, D. C., and Buhrman, R. A. (2011). Spin-torque ferromagnetic resonance induced by the spin Hall effect. Physical Review Letters, 106(3), 1-4.

Development of Operando Magnetic Device for Lorentz Transmission Electron Microscopy

CNF Project Number: 2091-11

Principal Investigator(s): Gregory D. Fuchs, David A. Muller

User(s): Albert M. Park

Affiliation(s): Applied Physics, Cornell University

Primary Source(s) of Research Funding: Defense Advanced Research Projects Agency (DARPA)

Contact: gdf9@cornell.edu, amp356@cornell.edu

Primary CNF Tools Used: GCA 5X stepper, wet stations, CVC evaporators, Heidelberg mask writer, dicing saw

Abstract:

We develop a magnetic device for operando Lorentz transmission electron microscope (LTEM) studies of magnetic skyrmions under the application of electric current pulses. We study the creation and annihilation of skyrmions in the presence of a strong pinning defect within a ferromagnetic multilayer with interfacial Dzyaloshinskii-Moriya interaction (DMI). We also show that Joule heating plays a primary role in this process. By controlling the magnetic field and total injected thermal energy, we can control the skyrmion density. Additionally, we study the relationship between skyrmion density and skyrmion stability to variations in the magnetic field. Our results show that the higher density skyrmions resist annihilation over a wider range of magnetic field.

Summary of Research:

Magnetic skyrmions are promising for potential high-performance memory and neuromorphic computing devices, however, to understand their behavior and dynamics at the smallest scales, a method of nanoscale imaging is essential [1,2]. To date, the study of chiral magnetic features in LTEM has been limited to operando changes of the magnetic field and temperature, with a few exceptions of single-crystalline samples, which were thinned and micropatterned by focus ion beam (FIB) for application of DC current [3-5]. To enable the study of skyrmion behavior with the application of electric current pulses, we develop a skyrmion device platform that is compatible with operando electrical biasing inside an electron microscope.

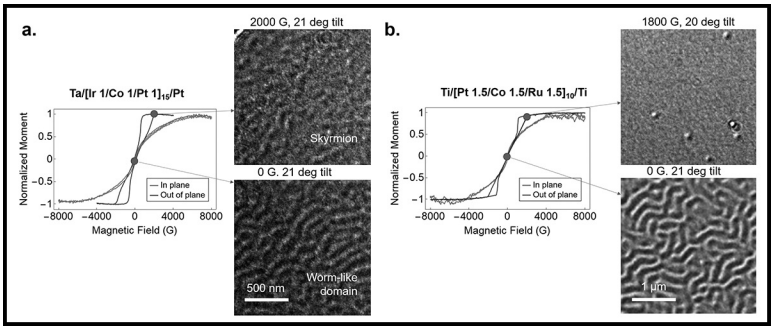

Figure 1: Magnetic hysteresis determined by vibrating sample magnetometry (VSM) and the LTEM image of spin textures for (a) Ta(2)/[Ir (1 nm)/Co (1 nm)/Pt (1 nm)]15 and (b) Ti(3)/[Pt (1.5 nm)/Co (1.5 nm)/Ru (1.5 nm)]10.

We start by optimizing the skyrmion materials. Two important micromagnetic interactions for stabilization of skyrmions in a thin-film multilayer structure are interfacial Dzyaloshinskii Moriya Interaction (DMI) and perpendicular magnetic anisotropy (PMA). We use platinum/cobalt (Pt/Co) bilayers to ensure PMA in our films. Iridium (Ir) or ruthenium (Ru) is used for the third layer because the interface on the opposite side of Pt in Pt/Co/Ir or Pt/Co/Ru trilayer is known to have an additive effect on effective DMI [6]. While we observe nucleation of skyrmions from both Pt/Co/Ir and Pt/Co/Ru stacks, we find that samples seeded from Ti/Pt or Ta/Pt on the membrane shows better LTEM contrast (Figure 1).

To enable an LTEM study of the chiral magnetic materials, we need to fabricate our device on an electron transparent material such as SiN_x membrane with a thickness of less than 100 nm. We use a Protochip™ fusion e-cell, which is composed of a 50 nm thick SiN_x

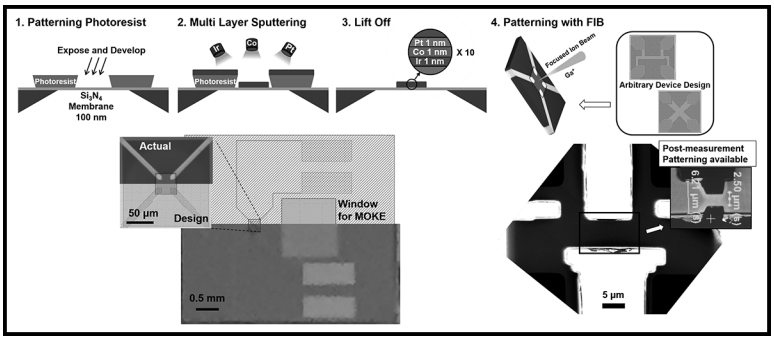

Figure 2: Fabrication process flow for the operando device. Optical image of Protochip™ fusion e-cell template overlaid with mask pattern for photolithography (left below) and a scanning electron micrograph of the device after patterning with FIB (right below). (See pages vi-vii for full color version.)

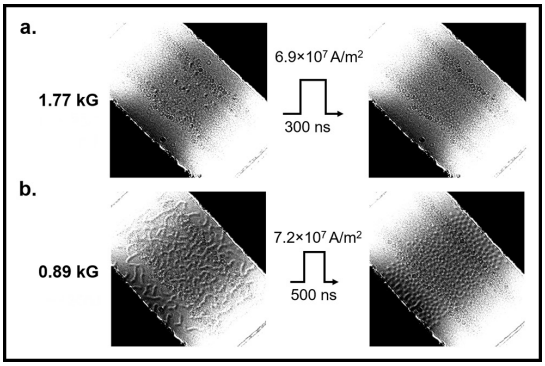

Figure 3: Current induced thermal annihilation (a) and nucleation (b) of skyrmions in the device.

membrane window with gold electrodes that extend toward the center of the membrane as a template to build our device. Multiple repeats of heavy metal/ferromagnet/heavy metal trilayer are deposited using an AJA sputter system (Figure 2). While micrometer-scale devices can be fabricated by lift-off alone, focused ion beam (FIB) can also be used as a post-processing method to define smaller features. We confirm that a versatile approach of defining a larger area of the film first and then direct writing a specific shape using FIB is possible.

Using the device, we observe thermal nucleation and annihilation of skyrmions induced by current-induced Joule heating (Figure 3) and quantify the energetics of the magnetic states with micromagnetic simulations. We find that the skyrmions are strongly bound to point-like pinning sites created by defects that are inherently present on the SiNx membrane provided by Protochip™. The thermal nucleation process enables the control of the skyrmion density choosing the magnetic field and the current pulse energy. Next, we investigate the stability of skyrmions as a function of their density. After systematically initializing a particular skyrmion density, we vary the magnetic field to find the magnetic field range that the skyrmions are stable. We find that while all skyrmions annihilate at high field regardless of the initial density, the lower bound of skyrmion stability is proportional to the initial skyrmion density.

Conclusions and Future Steps:

In conclusion, we have optimized a chiral material heterostructure and established a fabrication process for operando electron microscope studies of skyrmion creation and annihilation using electric current in the presence of strong magnetic pinning sites. We find that a thermal mechanism dominates these processes and that the resulting skyrmions have density-dependent stability. Understanding this mechanism has implications for controlling the density of skyrmions in devices. Additionally, operando transport properties such as the topological Hall effect and its relation to the nature of the chirality and the pinning effects can be investigated in the future based on this platform.

References:

[1] X. Zhang, Y. Zhou, K. Mee Song, T. Park, J. Xia, M. Ezawa, X. Liu, W. Zhao, G. Zhao, and S. Woo, J. Phys. Condens. Matter 32, 143001 (2020).

[2] N. Nagaosa and Y. Tokura, Nat. Nanotechnol. 8, 899 (2013).

[3] X. Z. Yu, N. Kanazawa, W. Z. Zhang, T. Nagai, T. Hara, K. Kimoto, Y. Matsui, Y. Onose, and Y. Tokura, Nat. Commun. 3, (2012).

[4] X. Z. Yu, Y. Tokunaga, Y. Kaneko, W. Z. Zhang, K. Kimoto, Y. Matsui, Y. Taguchi, and Y. Tokura, Nat. Commun. 5, (2014).

[5] L. Peng, Y. Zhang, M. He, B. Ding, W. Wang, H. Tian, J. Li, S. Wang, J. Cai, G. Wu, J. P. Liu, M. J. Kramer, and B. G. Shen, Npj Quantum Mater. 2, 1 (2017).

[6] D. Khadka, S. Karayev, and S. X. Huang, J. Appl. Phys. 123, 123905 (2018).

Frequency Domain Measurements of Arrays of Constriction-Based Spin-Hall Nano-Oscillators in Weak In-Plane Fields

CNF Project Number: 2091-11

Principal Investigator(s): Gregory D. Fuchs

User(s): Yanyou Xie

Affiliation(s): Applied and Engineering Physics, Cornell University

Primary Source of Research Funding: National Science Foundation

Contact: gdf9@cornell.edu, yx322@cornell.edu

Primary CNF Tools Used: JEOL 9500, MA6 contact aligner

Abstract:

Spin-Hall nano-oscillators (SHNOs) convert D.C. charge current to microwave frequency magnetic oscillations — enabling applications as highly agile microwave sources. The use of SHNOs for applications is still limited by low output microwave power and large linewidth. Mutual synchronization of arrays of constriction-based SHNOs under out-of-plane magnetic fields close to 1 T [1] have been studied as a route to improve these characteristics. However, such high magnetic fields are impractical for device applications. Therefore, we study mutual synchronization in devices under in-plane magnetic fields of tens of mT. We fabricated arrays of four constriction-based SHNOs with different geometries, and performed frequency domain measurements under varied bias current and magnitude of magnetic field.

Summary of Research:

The spin Hall effect (SHE) is the generation of transverse spin currents by electric currents; in a non- magnetic material (NM), this leads to the accumulation of spins with opposite polarization at opposite edges of the NM [2,3]. By placing a nonmagnetic film on top of a ferromagnetic film, the spin current generated in the NM can diffuse into the ferromagnet (FM), providing spin transfer torque (STT) to the FM [2]. Under suitable conditions, the STT is able to compensate the damping of magnetic precession, leading to steady precession of magnetization [4]. With this principle, spin-Hall nano-oscillators (SHNOs) are developed as a bilayer system consisting of NM and FM, patterned as nanowires or nanoconstrictions.

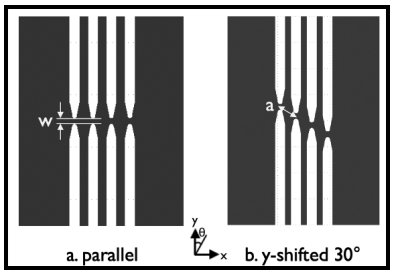

Figure 1: Central areas of SHNOs studied: (a) in-line constrictions (b) constrictions with a lateral shift.

In our study, we fabricated arrays of four $Ni_{81}Fe_{19}$ (5 nm)/$Au_{0.25}Pt_{0.75}$ (5 nm) constriction-based SHNOs on 20.5 μm × 4 μm wires, with different constriction width, separation and lateral shift. We used JEOL 9500 for the e-beam patterning of the SHNOs, and MA6 contact aligner and evaporator for depositing contact pads for electrical measurements. We measured the auto-oscillations of two devices. Each has a constriction width w = 100 nm, constriction separation a = 550 nm, however, one has in-line constrictions (Figure 1a), and the other with a lateral shift of the constrictions corresponding to a 30° angle (Figure 1b).

To measure the auto-oscillations, we apply a D.C. charge current to the device under a static in-plane magnetic field. Magnetic precession is induced in the FM ($Ni_{81}Fe_{19}$) due to SHE, leading to the oscillation of the FM layer's resistance due to anisotropic magnetoresistance. The oscillation signals are then measured using a spectrum analyzer with a pre-amplifier.

For the device with a lateral shift, we observed a single dominant peak over a range of currents at external

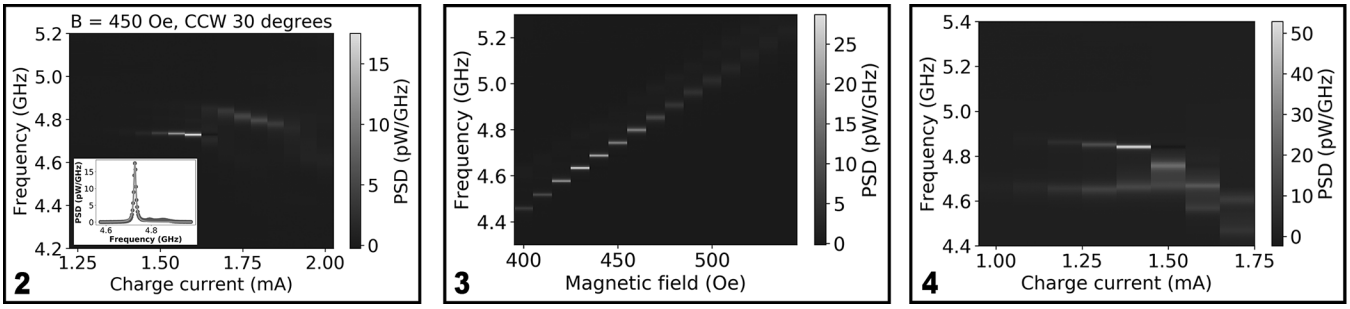

Figure 2, left: *Power spectral density (PSD) of device with lateral shift under* H *= 450 Oe with* θ *= 30°. Inset: the peak profile at 1.6 mA (dots) with Lorentzian fit (line).* ***Figure 3, middle:*** *PSD of device with lateral shift under a magnetic field with* θ *= 30° and charge currents of 1.6 mA.* ***Figure 4, right:*** *PSD of device with in-line constrictions under* H *= 450 Oe with* θ *= 30°. (See pages vi-vii for full color versions.)*

magnetic field H = 450 Oe applied θ = 30° with respect to the y axis (Figure 2). The angle of magnetic field accounts for the directionality of the spin wave emission perpendicular to the magnetic field [5]. By fitting the peak with a Lorentzian (Figure 2 inset), we extrapolate the linewidth of the optimal peak to be 10.8 MHz and the total power to be 0.2 pW, which is comparable to a prior report [6] in devices with similar resistance. We also observe a jump in the oscillation frequency, which is possibly due to the switching of dynamic modes [7]. At 1.6 mA bias current, the auto-oscillation frequency increases linearly with H; only one dominant peak occurs (Figure 3), suggesting that there may be some synchronization [1]. However, to verify whether the SHNOs are actually mutually synchronized, a study of the phase difference between them is required.

We also measured the auto-oscillation on the device with in-line constrictions under the same external magnetic field (Figure 4). In this case, two modes are observed at the same bias current, suggesting that the SHNOs are not synchronized.

Conclusions and Future Steps:

We performed frequency domain measurements on two of the fabricated devices, however, we have not yet experimentally confirmed mutual synchronization. Future studies using optical imaging techniques may reveal the phase information of the individual SHNOs. We also plan to study devices with smaller separation between constrictions, which we expect to synchronize robustly.

References:

[1] A. Awad, et al., "Long-range mutual synchronization of spin hall nano-oscillators," Nature Physics, vol. 13, no. 3, pp. 292-299, 2017.

[2] J. Sinova, et al., "Spin hall effects," Reviews of Modern Physics, vol. 87, no. 4, p. 1213, 2015.

[3] M. D'yakonov and V. Perel, "Possibility of orienting electron spins with current," Soviet Journal of Experimental and Theoretical Physics Letters, vol. 13, p. 467, 1971.

[4] D. C. Ralph and M. D. Stiles, "Spin transfer torques," Journal of Magnetism and Magnetic Materials, vol. 320, no. 7, pp. 1190-1216, 2008.

[5] T. Kendziorczyk and T. Kuhn, "Mutual synchronization of nanoconstriction-based spin Hall nano-oscillators through evanescent and propagating spin waves," Physical Review B, vol. 93, no. 13, p.134413, 2016.

[6] H. Mazraati, et al., "Low operational current spin Hall nano-oscillators based on NiFe/W bilayers," Applied Physics Letters, vol. 109, no. 24, p. 242402, 2016.

[7] J. Sankey, et al., "Mechanisms limiting the coherence time of spontaneous magnetic oscillations driven by dc spin-polarized currents," Physical review B, vol. 72, no. 22, p. 224427, 2005.

Imaging Nanoscale Magnetization Using Scanning-Probe Magneto-Thermal Microscopy

CNF Project Number: 2091-11

Principal Investigator(s): Gregory D. Fuchs

User(s): Chi Zhang

Affiliation(s): Applied and Engineering Physics, Cornell University

Primary Source(s) of Research Funding: Air Force Office of Scientific Research (FA9550-14-1-0243)

Contact: gdf9@cornell.edu, cz435@cornell.edu

Primary CNF Tools Used: JEOL 9500, GCA 5x stepper

Abstract:

High resolution, time-resolved magnetic microscopy is crucial for understanding novel magnetic phenomenon such as skyrmions, spinwaves, and domain walls. Currently, achieving 10-100 nanometer spatial resolution with 10-100 picosecond temporal resolution is beyond the reach of table-top techniques. We have developed a time-resolved near field magnetic microscope based on magneto-thermal interactions, which achieved spatial resolution of sub-100 nm. Our results suggest a new approach to nanoscale spatiotemporal magnetic microscopy in an accessible, table-top form to aid in the development of high-speed magnetic devices.

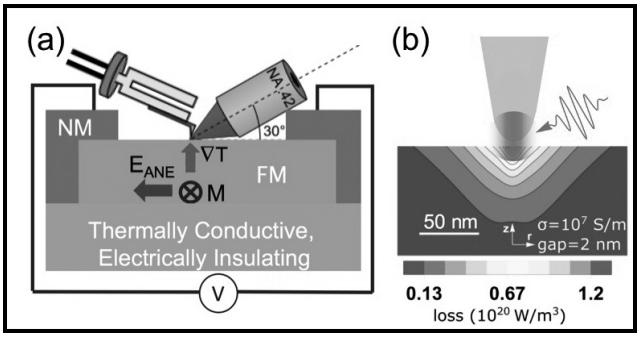

Figure 1: Schematics of (a) our scanning near field magneto-thermal microscopy setup, illustrating laser, sample and scan probe, and (b) near-field interaction. The sample figure in (b) is from Ref. [5].

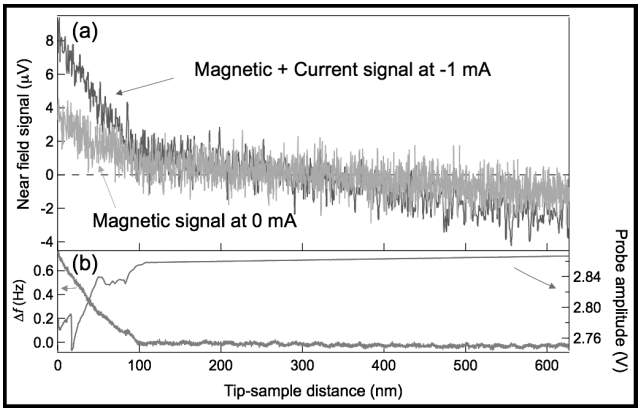

Figure 2: Near-field characteristic. Tip-sample distance dependence of (a) near-field signals and (b) probe parameters.

Summary of Research:

Our group has previously developed a time-resolved magneto-thermal microscopy [1-3]. We apply a pulsed laser to create thermal gradient ∇T. The local magnetization M subjected to ∇T generates an electric field E_{ANE} through anomalous Nernst effect [Figure 1(a)]. This enables us to do magnetic imaging, with a spatial resolution of 650 nm and a temporal resolution of 10 ps. This technique can be used to image both local static and dynamic magnetization, as well as an applied current density [4]. In this work, we extend the magneto-thermal microscopy to nanoscale resolution with near-field light. We use a gold-coated cantilever glued on tuning fork as our probe, controlled by atomic force microscopy.

We shine a laser on the tip apex, and the near field enhancement of the electric field at the tip [5-6] heats the sample as a nanoscale heat source [Figure 1(b)]. The heating length scale is comparable to the tip radius; below 100 nm.

We first study a 5 μm × 15 μm CoFeB/Hf/Pt sample fabricated using photolithography with the GCA 5x stepper. We confirm the near-field characteristic of the signal by measuring as a function of tip-sample distance. We record the near-field signal as well as other probe parameters as the tapping probe approaches the sample [Figure 2]. The near-field signal increases when the tip

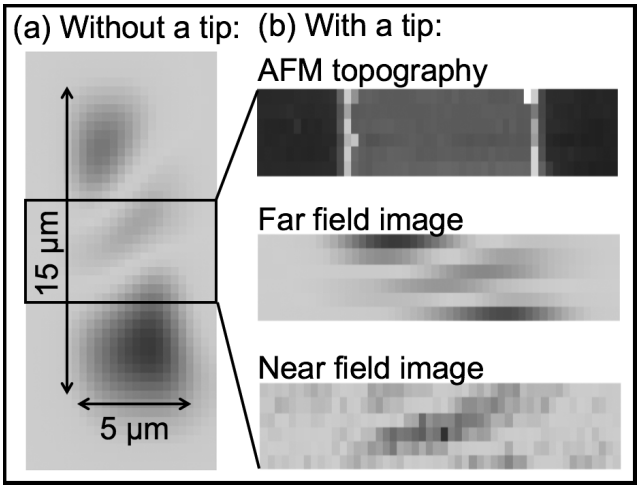

Figure 3: Magnetic multi-domain imaging. (a) Magnetic far-field images of a multi-domain state. (b) With a scanning probe tip, topography, far-field and near-field images acquired simultaneously.

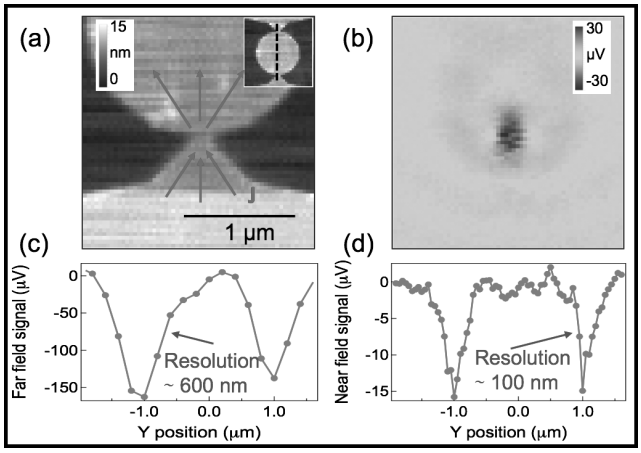

Figure 4: Current imaging and spatial resolution. (a) Topography and (b) current density images acquired by a near field tip. Line cuts through two necks (as illustrated in the inset of (a)) of (c) far field and (d) near field signals for resolution comparison.

is in first contact with the sample, indicated by an initial increase of the frequency and decrease of the amplitude. The short-range nature of the signal is consistent with a near-field interaction.

We next demonstrate magnetic imaging of near field scanning probe with a multi-domain state. Figure 3(a) shows a far-field image taken by a focused light to confirm the magnetic state. Figure 3(b) shows topography, far-field and near-field images, acquired simultaneously with the scanning probe. The near-field image resembles the far-field image, but with higher resolution. We note that the near-field image has a smallest feature of ~ 300 nm in this sample, which is below the optical diffraction limit of the set-up. That feature is likely the actual domain wall width rather than being limited by the instrument resolution.

To probe instrument resolution further, we measure in current imaging mode and use a new sample designed with a sharp current density feature. The sample is a thin-film heterostructure composed of 5 nm $Ni_{81}Fe_{19}$/2 nm Ru, then patterned into a 2-μm-diameter disk with two 130 nm necks using JEOL 9500 e-beam lithography. Figure 4 shows topography and near-field current density images taken with the near-field scanning probe. By taking linecuts through two necks, as shown in Figure4(a) inset, we compare signals between focused light far field and scanning probe near field. The scanning near-field image has higher resolution than far field image, and based on sharp features, demonstrates an upper bound of spatial resolution of 100 nm.

Conclusions and Future Steps:

We have developed a time-resolved scanning near field magneto-thermal microscopy for magnetic and current imaging. We confirmed near field nature of the signal, and characterized the spatial resolution to be sub-100 nm. In the future, we will apply this instrument to study the dynamics of nanoscale spin textures.

References:

[1] J. M. Bartell, D.H. Ngai, et al., Nat. Commun. 6, 8460 (2015).

[2] J. M. Bartell, et al., Phys. Rev. Appl. 7, 044004 (2017).

[3] I. Gray, et al., Phys. Rev. Mater. 3, 124407 (2019).

[4] F. Guo, et al., Phys. Rev. Appl. 4, 044004 (2015).

[5] J. C. Karsch, et al., APL Photonics 2, 086103 (2017).

[6] L. Meng, et al., Optics Express, 11, 13804, (2015).

Magnetic Resonance Force Detection and Imaging of Electron Spins in a Laminate Thin Film

CNF Project Number: 2125-12

Principal Investigator(s): John Marohn

User(s): Michael Boucher

Affiliation(s): Department of Chemistry and Chemical Biology, Cornell University

Primary Source(s) of Research Funding: Army Research Office

Contact: john.marohn@cornell.edu, mcb344@cornell.edu

Website: marohn.chem.cornell.edu

Primary CNF Tools Used: SC 4500 Combination Thermal/E-gun Evaporation System, Zeiss Supra SEM

Abstract:

Magnetic resonance force microscopy (MRFM) is a nanoscale imaging technique that uses a force sensor such as a cantilever, nanowire, or membrane, along with a field gradient to detect magnetic resonance and spatially resolve spins. The Marohn group is interested in using MRFM to image soft materials such as membrane proteins and other biomolecules. Detection of a few hundred nuclear spins or one electron and resolution of less than a nanometer have been demonstrated [1-3]. The Marohn group uses equipment at the Cornell NanoScale Facility (CNF) and the Cornell Center for Materials Research (CCMR) to produce cantilevers with nanomagnet tips as well as waveguides to deliver radio- and microwave frequency radiation to manipulate sample spins. In a previous report we detailed sample preparation methods we had developed to reduce noise due to sample charge fluctuations while avoiding sample damage. In this report we provide an update on measurement experiments performed on the sample prepared using our newly developed techniques.

Summary of Research:

Using a protocol developed at the CNF, the Marohn group fabricated attonewton-sensitivity cantilevers and nanomagnets that were affixed to the leading edge using a STEM-FIB system at the CCMR. An experiment on a 40 nm thin film demonstrated 500 proton-sensitivity in a mHz bandwidth [1], a sensitivity equivalent to that required for single electron radical imaging.

In our report for the 2017-2018 CNF Research Accomplishments, we described experiments performed on a 200 nm thick polystyrene thin film doped to 40 mM with 4-amino-TEMPO, a nitroxide radical. Our detection scheme modulates the sample electron spin polarization and detects the change in magnetization as a modulated shift in the cantilever frequency. To minimize cantilever frequency noise from fluctuating sample charges, we used e-beam evaporation to apply a 10 nm layer of gold to the polystyrene sample surface (SC 4500 Combination Thermal/E-gun Evaporation System). Based on our experimental measurements and later conventional ESR of test films, however, we believe that a 20 nm thick layer of the sample is destroyed by the gold deposition. This "dead layer" increases the standoff distance between the magnet tip and sample spins being measured, making it difficult to do single electron detection in a practical measurement time. In our previous report we presented a new "laminate" sample preparation technique that protects the cantilever from sample charge fluctuations without exposing sample nitroxide radicals to direct exposure from physical vapor deposition of metals (Figure 1).

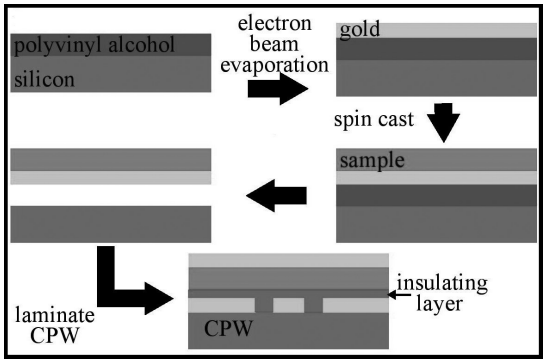

Figure 1: An outline of the sample/top contact transfer process which allows samples to be produced without exposing sensitive nitroxide electron radicals to physical deposition of the gold top contact.

In May-June 2019 we performed experiments on one of these laminate samples using a magnet-tipped cantilever prepared by epoxying a 4-micron-diameter spherical nickel magnet to one of our CNF-fabricated cantilevers. This larger tip reduces per-spin sensitivity of our system but puts more spins in resonance at a given microwave frequency, allowing us to more easily test and calibrate our system.

Our first measurement was to scan the irradiation frequency at a variety of tip-sample separations. This provides us with the tip-field at each separation, tells us about the field-gradient, and lets us fit the result to an analytical model of a spherical magnet (Figure 2).

We also used MRFM to detect the spin-lattice relaxation time T1 of sample spins using a "phase-kick" protocol described by Moore, et al. [4]. Our measured values match Moore's and provide evidence that the laminate sample preparation does not degrade the sample (Fig.3).

Another test of our setup was to perform a proof-of-concept imaging experiment. In theory our sample should not be interesting to image, being a uniform thin film with a constant dopant concentration. However, we found a protuberance in the sample that we could measure. We scan laterally over the sample in small steps to form a 12 × 12 grid. We also vary the irradiation frequency to change the shape of the resonant slice. As the resonant slice scans over the protuberance, it adds to the signal observed at that grid point. By changing the irradiation frequency, we change the radius of the resonant slice and therefore the size of the rings of increased signal (Figure 4). We expect imaging of smaller scale objects to behave in a similar manner.

Future work will involve using a smaller magnet tip to continue imaging experiments on samples with nanoscale features of interest for imaging.

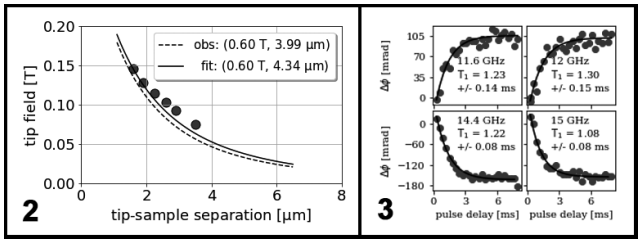

Figure 2, left: *Tip field versus tip-sample separation along with a fit to an analytical magnet field for a spherical model.* ***Figure 3, right:*** *Cantilever phase shift versus pulse delay measured at different irradiation frequencies. Inset shows best fit spin-lattice relaxation time.*

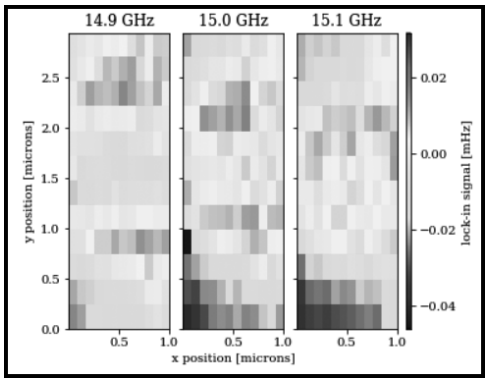

Figure 4: Map of spin-induced cantilever frequency shift at various irradiation frequencies. Step size: Δx = 91 nm, Δy = 258 nm. (See pages vi-vii for full color version of figure.)

References:

[1] Longenecker, et al. ACS Nano 2012, 6 (11), 9637-9645.

[2] Rugar, et al. Nature 2004, 430 (6997), 329-332.

[3] Grob, et al. Nano Letters 2019, 19 (11), 7935-7940.

[4] Moore, et al. PNAS 2009, 106 (52), 22251-22256.

Acoustically Driving the Single Quantum Spin Transition of Diamond Nitrogen-Vacancy Centers

CNF Project Number: 2126-12

Principal Investigator(s): Gregory D. Fuchs[1]

User(s): Huiyao Chen[2], Johnathan Kuan[2]

Affiliation(s): 1. School of Applied and Engineering Physics, 2. Department of Physics; Cornell University

Primary Source(s) of Research Funding: DARPA DRINQS program (Cooperative Agreement #D18AC00024); Office of Naval Research (Grants No. N000141712290)

Contact: gdf9@cornell.edu, hc846@cornell.edu, jk2788@cornell.edu

Website: http://fuchs.research.engineering.cornell.edu

Primary CNF Tools Used: PT770 etcher, GCA 5x stepper, Heidelberg mask writer DWL2000, AJA sputtering deposition System, odd/even evaporator, YES asher, P10 profilometer, Westbond 7400A ultrasonic wire bonder

Abstract:

Using a high quality factor 3 GHz bulk acoustic wave resonator device, we demonstrate the acoustically driven single quantum (SQ) spin transition ($|m_s = 0\rangle \leftrightarrow |\pm 1\rangle$) for diamond nitrogen-vacancy (NV) centers and characterize the corresponding stress susceptibility. We find that the SQ spin-stress coupling is comparable to that for double quantum (DQ) transition, about an order of magnitude larger than a theoretical prediction. This work further completes our understanding of the NV spin-stress Hamiltonian and enables all-acoustic spin control of NV center spins.

Summary of Research:

Acoustic control of diamond nitrogen-vacancy (NV) center spins provides additional resources for quantum control and coherence protection that are unavailable in conventional magnetic resonance approaches. While acoustically-driven double quantum spin transition has been widely studied, acoustically-driven single quantum spin transition is yet unexplored.

Here we report our experimental study of acoustically-driven SQ spin transitions of NV centers using a 3 GHz diamond bulk acoustic resonator device [1]. The device converts a microwave driving voltage into an acoustic wave through a piezoelectric transducer, thus mechanically addressing the NV centers in the bulk diamond substrate (Figure 1). Because a microwave current flows through the device transducer, an oscillating magnetic field of the same frequency coexists with the stress field that couples to SQ spin transitions.

To identify and quantify the mechanical contribution to the SQ spin transition, we use Rabi spectroscopy to separately quantify the magnetic and stress fields present in our device as a function of driving frequency. The results are shown in Figure 2. Based on these results, we construct a theoretical model and simulate the SQ spin transition Rabi spectroscopy to compare to the experimental results. From a systematically identified closest match (Figure 3), we quantify the mechanical driving field contribution and extract the effective spin-stress susceptibility, b'. We perform measurements on both the $|0\rangle \leftrightarrow |+1\rangle$ and $|0\rangle \leftrightarrow |-1$. SQ spin transitions and obtain $b'/b = \sqrt{2}(0.5 \pm 0.2)$, where b is the spin-stress susceptibility of DQ transition.

The fact that b' is comparable to b, about an order of magnitude larger than expected theoretically [2], has important implications for applications. It raises the possibility of all-acoustic spin control of NV centers within their full spin manifold without the need for a magnetic antenna. For sensing applications, a diamond bulk acoustic device can be practical and outperform a microwave antenna in several aspects: 1) Acoustics waves provide direct access to all three qubit transitions, and the DQ qubit enables better sensitivity in magnetic metrology applications; 2) The micron-scale phonon wavelength is ideal for local selective spin control of NV centers; 3) Bulk acoustic waves contain a uniform stress mode profile and thus allows uniform field control of a large planar spin ensemble, for example, from a delta-doped diamond growth process.

This study [3], combined with previously demonstrated phonon-driven DQ quantum control and improvements in diamond mechanical resonator engineering, shows that diamond acoustic devices are a powerful tool for full quantum state control of NV center spins.

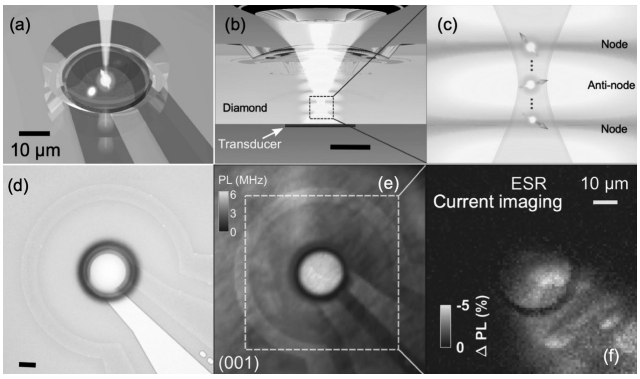

Figure 1: (a) and (b) are concept images of the device side view and cross-sectional view. An NA = 0.8 objective focuses the 532 nm laser down into diamond at a depth close to the transducer (around 3 μm in distance). The orange standing wave field illustrates the acoustic wave mode. (c) Closeup of the area under study. (d) and (e) are optical image and photoluminescence scan of the device, consisting of a semi-confocal diamond bulk acoustic resonator (center bright region) and a 50 μm radius microwave loop antenna. (f) Electron spin resonance signal mapping of the device current field around the resonator, showing current flow primarily along the electrodes.

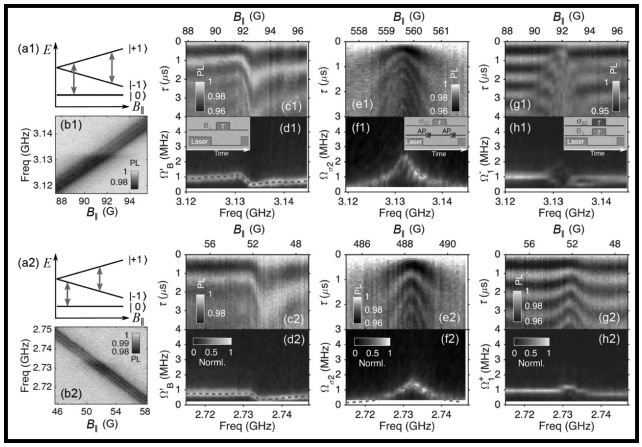

Figure 2: Spectroscopy study of NV center spin under driving fields at frequencies near two acoustic modes at (1) 3.132 GHz and (2) 2.732 GHz. Ground-state spin level diagrams in (a1-a2) show the targeted DQ (orange arrow, $|-1\rangle \leftrightarrow |+1\rangle$) and SQ (blue arrow $|0\rangle \leftrightarrow |\pm1\rangle$) transitions within nuclear spin $|m_I = +1\rangle$ hyperfine manifold. Transducer driving creates both magnetic, $B_\perp$, and acoustic fields, σ_{zz}, in the device, which can be measured independently by (c) SQ Rabi spectroscopy near the leads and (e) DQ Rabi spectroscopy in the center of the resonator. In the resonator, the two vector fields add coherently and drive the SQ transition together. Measurements of the resulting total field probed by SQ ESR and Rabi spectroscopy are shown in (b) and (g), respectively. (d, f, h) are Fourier transforms of (c, e, g). The insets in (d1, f1, h1) show the corresponding measurement sequences.

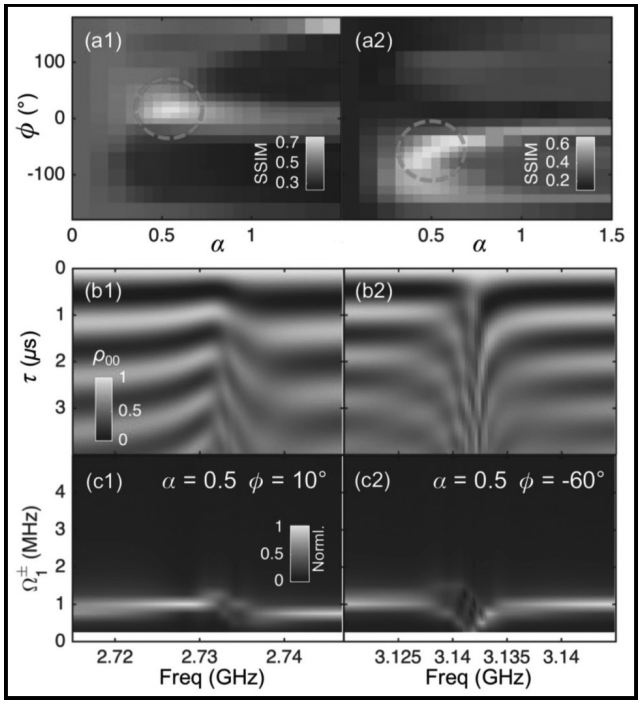

Figure 3: Quantum master simulation of SQ spin transition under dual field driving. (a1-a2) are heatmaps of structural similarity index measure between experimental data and simulation in {φ,α} parameter space for 2.732 GHz and 3.132 GHz mode, respectively. The dashed circles mark the locations of peak SSIM values. (b1-b2) The corresponding simulated Rabi spectroscopy results using the peak SSIM associated {φ,α} values match the experimental data in Figure 2g. (c1-c2) are Fourier transforms of (b1-b2).

References:

[1] H. Chen, N. F. Opondo, B. Jiang, E. R. MacQuarrie, R. S. Daveau, S. A. Bhave, and G. D. Fuchs, Nano letters 19, 7021 (2019).

[2] P. Udvarhelyi, V. O. Shkolnikov, A. Gali, G. Burkard, and A. Palyi, Physical Review B 98, 075201 (2018).

[3] H. Chen, S. Bhave, and G. Fuchs, arXiv preprint arXiv:2003.03418 (2020).

(See pages vi-vii for full color versions of all three figures.)

Shallow Diamond Silicon Vacancy Centers for Coherent Spin-Magnon Coupling

CNF Project Number: 2126-12

Principal Investigator(s): Gregory D. Fuchs[1]

User(s): Hil Fung Harry Cheung[2]

Affiliation(s): 1. School of Applied and Engineering Physics, 2. Department of Physics; Cornell University

Primary Source(s) of Research Funding: Department of Energy (Grants No. DE-SC0019250)

Contact: gdf9@cornell.edu, hc663@cornell.edu

Website: http://fuchs.research.engineering.cornell.edu

Primary CNF Tools Used: GCA 5x stepper, AJA sputtering deposition system, P10 profilometer, Westbond 7400A ultrasonic wire bonder, Veeco Icon atomic force microscope, PT770 etcher

Abstract:

We aim to develop a platform for coupling isolated silicon-vacancy (SiV) electron spins to magnetic spin waves, potentially enabling a magnon mode to act as a quantum bus. To enhance the dipolar coupling, SiV centers need to be placed near the magnetic material, and thus near the surface of the diamond. Here we report on our study of the optical properties of shallow diamond SiV centers.

Summary of Research:

Diamond SiV centers can have long spin coherence times and narrow optical transitions, enabling the realization of spin-photon entanglement [1]. These good properties make SiV a good candidate for engineering a quantum bus. We aim to develop a spin-magnon interface by coupling SiV centers to a high-quality magnon mode. A key parameter, the spin-magnon coupling rate, is maximized when the SiV spins are close to the magnetic material [2]. However, shallow defects are more susceptible to surface states that reduce coherence times and broaden optical transitions [3,4]. Here we fabricate near surface diamond SiV centers and study their properties relevant to spin-magnon transduction.

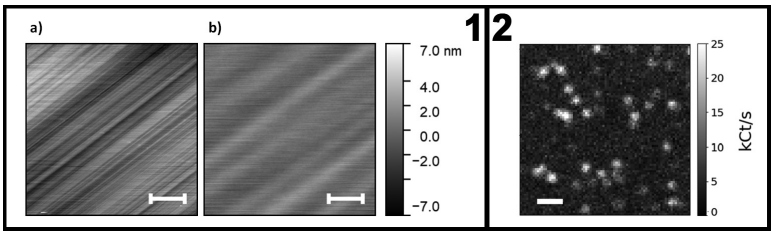

Figure 1, left: Diamond surface atomic force microscope (AFM) image before (a) and after (b) Ar/Cl2 and O2 reactive ion etch. Scale bar is 1 μm.

Figure 2, right: Photoluminescence image of SiV centers. Scale bar is 1 μm.

We start from a single crystal diamond substrate (nitrogen concentration < 5 ppb). A polished diamond sample has a highly strained surface layer. We remove the top 5 μm using reactive ion etch (RIE) with Ar/Cl_2 and O_2 plasma [5,6] using the PT 770 etcher. This process reduces surface roughness and polishing streaks (Figure 1). The diamond sample is then implanted with 45 keV ^{28}Si ion at a fluence 10^{10} ions/cm^2, resulting in an estimated implanted depth of 32 ± 9 nm [7]. The sample is vacuum annealed to mobilize vacancies enabling the formation of SiV centers. Vacuum annealing also leaves behind graphite on the diamond surface, which we remove by cleaning the diamond in through a tri-acid boil (equal volume of sulfuric, nitric and perchloric acid).

We study the optical properties of the SiV centers in a home-built confocal microscope setup. SiV centers are excited with a continuous wave green laser (532 nm) with a power density of about 50 mW/μm^2. We observed a SiV density of 0.5 SiV/μm^2, corresponds to a conversion efficiency of 0.5% (Figure 2), comparable to conversion efficiency at a higher implant energy (150 keV) [8].

SiV centers emit about 70% of light into the zero-phonon line (ZPL) near 737 nm [9], which is advantageous for single photon generation. At room temperature, this line is a few nm broad due to electron-phonon processes [10]. At low temperature (10 K), the line narrows and a four-line fine structure emerges (Figure 3a). The fluorescence wavelength distribution is shown in Figure 3b. About half of the SiV centers transition emission lines have linewidths at the spectrometer resolution limit.

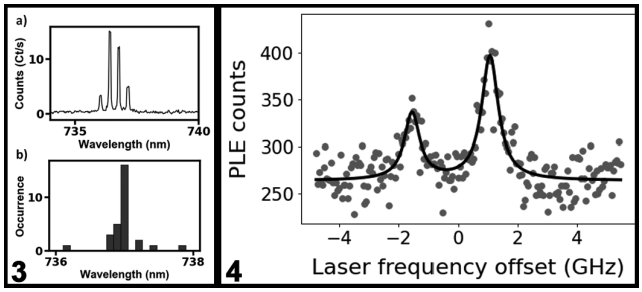

Figure 3, left: (a) Emission spectrum of a SiV center. (b) Wavelength distribution of 29 SiV centers. Figure 4, right: PLE scan of a SiV center under 400 nW/μm² resonant laser excitation. Full width half maximum (FWHM) are 630 ± 220 MHz and 680 ± 240 MHz.

To more accurately probe the linewidth, we use photoluminescence excitation (PLE) spectroscopy. We excite SiV centers with a frequency-tunable laser that we tune over the resonant optical transition while collecting emission from the phonon sidebands with wavelength larger than 750 nm. We observe narrow transition linewidths of 630 ± 220 MHz (Figure 4), which is only a few times larger than the lifetime limited linewidth (93 MHz) [8].

Conclusions and Future Steps:

We fabricated shallow diamond SiV centers with narrow optical transitions. In the future we plan to study the spin of shallow SiV centers as we work towards integration of SiV centers with magnetic material.

References:

[1] C. T. Nguyen, et al., "An integrated nanophotonic quantum register based on silicon-vacancy spins in diamond", Phys. Rev. B 100, 165428 (2019).

[2] D. R. Candido, et al., "Predicted strong coupling of solid-state spins via a single magnon mode", arXiv:2003.04341 (2020).

[3] B. A. Myers, et al., "Probing Surface Noise with Depth-Calibrated Spins in Diamond", Phys. Rev. Lett. 113, 027602 (2014).

[4] S. B. van Dam, et al., "Optical coherence of diamond nitrogen-vacancy centers formed by ion implantation and annealing", Physical Review B 99, 161203(R) (2019).

[5] Y. Chu, et al., "Coherent optical transitions in implanted nitrogen vacancy centers", Nano Lett. 14, 982 (2014).

[6] S. Sangtawesin, et al., "Origins of Diamond Surface Noise Probed by Correlating Single-Spin Measurements with Surface Spectroscopy", Phys. Rev. X 9, 031052 (2019).

[7] J. F. Ziegler, et al., "SRIM - The stopping and range of ions in matter (2010)", Nucl. Instrum. Methods Phys. Res., Sect. B 268, 1818 (2010).

[8] R. E. Evans, et al., "Narrow-Linewidth Homogeneous Optical Emitters in Diamond Nanostructures via Silicon Ion Implantation", Phys. Rev. Applied. 5, 044010 (2016).

[9] A. Dietrich, et al., "Isotopically varying spectral features of silicon vacancy in diamond", New J. Phys. 16, 113019 (2014).

[10] K. D. Jahnke, et al., "Electron-phonon processes of the silicon-vacancy centre in diamond", New J. Phys. 17, 043011(2015).

Quantum Emitters Activation in WSe_2 Monolayers via Hexagonal Boron Nitride Wrinkle Engineering

CNF Project Number: 2126-12

Principal Investigator(s): Gregory D. Fuchs

User(s): Raphael Sura Daveau, Tom Arno F. Vandekerckhove

Affiliation(s): Applied and Engineering Physics, Cornell University

Primary Source(s) of Research Funding: Air Force Office of Scientific Research (FA9550-18-1-0480)

Contact: gdf9@cornell.edu, rsd228@cornell.edu

Website: http://fuchs.research.engineering.cornell.edu

Primary CNF Tools Used: JEOL 6300 electron-beam writer, GCA 5x stepper, Oxford 81 etcher

Abstract:

Strain has been shown to be a key parameter to create quantum emitters in tungsten diselenide (WSe_2) monolayers. We report experimental observations of spatially and spectrally isolated single quantum emitters (QEs) in WSe_2 monolayers. We use hexagonal boron nitride (hBN) wrinkles nucleated from a nanostructured substrate to create strain at a size scale suitable to host single QEs, while avoiding other residual emission. In comparison, QEs stemming from direct strain points from the substrate yield multiple QEs per site and increased unwanted background emission.

Summary of Research:

Monolayer transition metal dichalcogenides are direct bandgap semiconductors with a strong light-matter interaction and possessing a new electronic degree of freedom, known as valley, that locks excitons to a given photon helicity [1]. Tungsten diselenide (WSe_2) has been shown to host bright and stable QEs [2]. While most reported emitters in WSe_2 monolayers are located at random, few reports show deterministic activation of QEs via local strain by placing the WSe_2 monolayer over a patterned substrate, in the form of nanopillars [3]. Strain engineering of WSe_2 monolayers is key to create QEs on demand and with position control [4].

Our approach uses a nano-patterned substrate as an indirect means to communicate strain to WSe_2 via a thin hBN layer, which appears to be suitable to create single QEs. In this work, we use a substrate patterned with nanopillars [3,4] and make a comparative study of emitters forming directly on the pillars versus along hBN wrinkles that propagate between pillars.

The nanopillars are fabricated from a SiO_2 substrate via electron-beam lithography (JEOL 6300) using M-aN 2403 negative resist. The nanopillars are etched into SiO_2 and are cylindrical with a diameter of 200 nm and height of 300 nm. Exfoliated WSe_2 monolayers and hBN are transferred using a polycarbonate (PC) on polydimethylsiloxane (PDMS) stamp technique. We study the samples using a homebuilt confocal microscopy setup with a 637 nm continuous wave laser at 10 K.

Figure 1 shows an atomic force micrograph (AFM) of a sample consisting of a hBN/WSe_2 heterostructure on a SiO_2 nanopillar substrate. The photoluminescence map from this sample shows that WSe_2 on the nanopillar (indicated with a large circle in Figure 1) emits most intensity because of the high strain while a less intense spot is visible along a hBN wrinkle (small circle in Fig.1).

The spectrum collected from the center of the nanopillar is shown in Figure 2 and shows two sharp features along with a broad emission from 755 nm to 775 nm.

Figure 3 on the other hand shows a spectrum taken on the wrinkle (see small circle in Fig.1). This spectrum features a single sharp peak at 765.8 nm with minimal background emission surrounding the peak. The AFM image reveals a kink in the wrinkle, i.e., increased strain, which can explain the creation of a quantum emitter at this specific site. At this location, the wrinkle is 90 nm high and has a full-width at half-maximum (FWHM) of 160 nm. The collected light from this spot is filtered through a 3 nm bandpass filter and sent to a Hanbury-Brown-Twiss interferometer for auto-correlation measurement. The time correlation between the two APD signals for the wrinkle QD is plotted as $g^{(2)}(t)$ in the

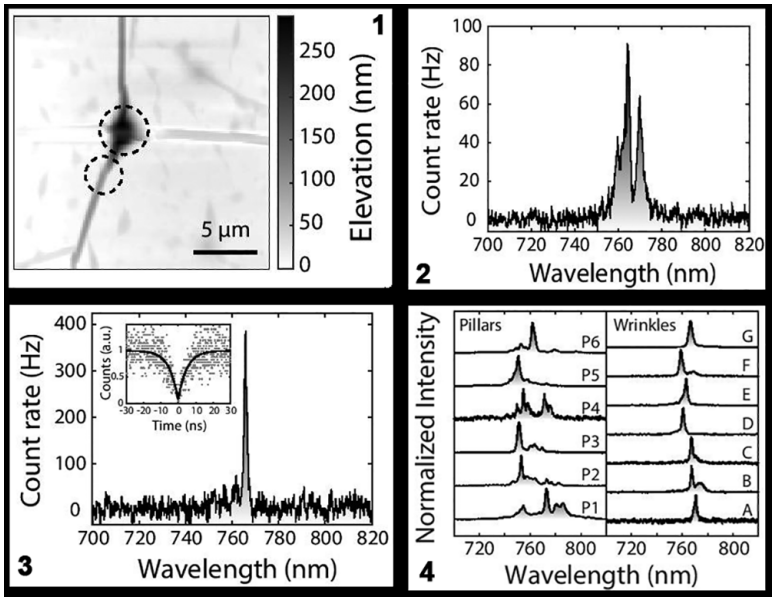

Figure 1: *Atomic force micrograph of the sample consisting of a WSe_2/hBN heterostructure on top of SiO_2 nanopillar substrate. Pillars bring most strain to WSe_2, however, hBN wrinkles bring more subtle strain suitable for creating cleaner single quantum emitters.* ***Figure 2:*** *Spectrum of light collected from the top of the nanopillar. Several peaks on top of a broad background are visible.* ***Figure 3:*** *Spectrum of light collected from the wrinkle, as circled in Fig.1. One clean peak is visible, meaning a single quantum emitter is created at this spot. Inset: second-order correlation function demonstrating the single-photon nature of the emission.* ***Figure 4:*** *(left) Spectra collected from the top of 300-nm high nanopillars. (right) Spectra collected from emission centers located along hBN wrinkles. The spectra systematically display a single peak and lower background level.*

inset of Figure 3. From the fit we extract $g^{(2)}(0)$ = 0.087, demonstrating the single-photon nature of the emission.

The spectrum of Figure 2 does not allow us to quantify $g^{(2)}(0)$ for the signal coming from the top of the nanopillar.

In another sample, we have studied six nanopillar-based QEs and seven wrinkle-based QEs. The spectra collected from the top of the pillars are shown in Figure 4 (left panel) and display one or several lines attributed to QEs and a broad emission background. In contrast, spectra that are collected along hBN wrinkles away from the pillars, shown in Figure 4 (right panel), consistently display a single peak, i.e., a single quantum emitter probed at a time, while the background level is significantly reduced.

We study the amount of background light emitted at the same frequency of the emitters on a 3~nm spectral window to quantify the effect on single-photon purity. We find that 25% of the signal is composed of unwanted background light for nanopillar-based emitters whereas this number is 15% for wrinkle-based emitters in comparison. This latter result intrinsically increases single-photon purity of wrinkle-based QEs.

Conclusions and Future Steps:

The use of a nano-patterned substrate to indirectly induce hBN wrinkles, may be a good choice to create single WSe_2 QEs with low background. Emitters created with hBN wrinkles are spectrally isolated from other emitters and have an increased single-photon purity, which is an advantage for application purposes. Future work should address the deterministic positioning of QEs along hBN wrinkles.

References:

[1] K. F. Mak and J. Shan, Nat. Photonics 10, 216 (2016).

[2] A. Srivastava, M. Sidler, A. V. Allain, D. S. Lembke, A. Kis and A. Imamo.lu, Nat. Nanotechnology 10, 1038 (2015).

[3] C. Palacios-Berraquero, D. M. Kara, A. R.-P. Montblanch, M. Barbone, P. Latawiec, D. Yoon, A. K. Ott, M. Loncar, A. C. Ferrari and M. Atature, Nat. Comm. 8, 15093 (2017).

[4] A. Branny, S. Kumar, R. Proux, and B. D. Gerardot, Nat. Comm. 8, 1-7 (2017).

Fabrication of Nanophotonic Optical Cavity Device from Inverse Design

CNF Project Number: 2126-12

Principal Investigator(s): Gregory D. Fuchs[1]

User(s): Jialun Luo[2]

Affiliation(s): 1. School of Applied and Engineering Physics, 2. Department of Physics; Cornell University

Primary Source(s) of Research Funding: National Science Foundation (ECCS-1839196)

Contact: gdf9@cornell.edu, JL3562@cornell.edu

Website: http://fuchs.research.engineering.cornell.edu

Primary CNF Tools Used: AJA sputtering system, OEM Endeavor AlN sputtering system, JEOL 9500, PT770 etcher, P10 profilometer, GCA 5x stepper

Abstract:

On-demand polarized single-photons are essential in realizing many photon-based quantum communication protocols. We are developing and fabricating a nanophotonic cavity device from aluminum nitride (AlN) to serve as a platform for enhancing single-photon emission from isolated defects hosted in hexagonal boron nitride. The target structure is designed via numerical optimization known as the inverse design. We present an update on our work-in-progress on the fabrication of the device.

Summary of Research:

Hexagonal boron nitride (hBN) has drawn a lot of attention recently because of its bright emission of single photons [1]. The defect emission is stable at room temperature and appears in the visible spectrum [2]. Researchers have been able to find or create isolated defects, making these defects promising candidates for implementing single-photon emitters that are important for quantum communication protocols [3]. In this project, we aim to develop bright, on-demand single-photon emitters using hBN defects. To enhance the emissions we fabricate a nanophotonic cavity device based on inverse design techniques [4]. The structure is designed such that it resonates at frequencies of the emission of the single emitters with a small mode volume.

We take advantage of the similarity in the index of refraction of hBN and aluminum nitride (AlN). Starting from a fused silica wafer, we sputter a 300 nm thick AlN layer using the OEM Endeaver M1 AlN sputter system. In particular, the nanophotonic cavity design has a 600 nm mode that is strongly confined in the center of the structure, thus aiming to enhance the emission rate of isolated defects at that frequency.

The process flow is outlined as follows (Figure. 1). We use the AJA sputter system to deposit a thin layer (of 20 to 30 nm) of chromium (Cr) on top of AlN. The Cr layer serves as a hard mask for the etching AlN. The patterning is done with electron beam lithography (EBL) with the JEOL 9500 and reactive ion etching (RIE) with the PT770 etcher. We choose hydrogen silsesquioxane (HSQ) diluted into 3% solution as the EBL resist due to its sub-10 nm resolution. HSQ is spun on the wafer with a thickness of 10 to 15 nm, which implies an aspect ratio of 1:2 for the subsequent etching of Cr. To avoid charging artifacts on the HSQ resist during exposure, we spin a layer of water-soluble discharge polymer on top of the HSQ. We write the device structure with JEOL 9500. Next, we develop the exposed HSQ in MIF 300 for one minute, rinse with DI water, and then blow dry. The subsequent etching steps are carried out in the PT770 etcher. We etch the Cr layer with Cl_2/O_2 plasma and then the AlN layer with Cl_2 plasma. Lastly, the Cr layer is removed by wet chemical etch.

This project is a work-in-progress as we are debugging the etching step of the AlN layer. The SEM image of the Cr mask of the pattern is shown in Figure 2. The smallest feature size is of 10 nm.

Future Steps:

We will complete and refine the process parameters to fabricate the nanophotonic cavity devices. We will study the optical properties of the devices and characterize the Purcell enhancement of single emitters coupled to the devices.

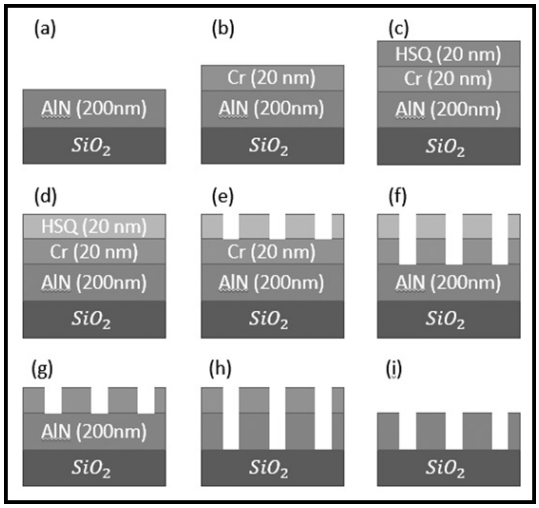

Figure 1: Outline of the process flow. (a-b) Sputtering of AlN and Cr on fused silica wafer, (c) deposition of HSQ, (d-e) EBL patterning on HSQ and development, (f) etching of Cr hard mask, (g) removal of HSQ, (h) etching of AlN, (i) removal of Cr mask.

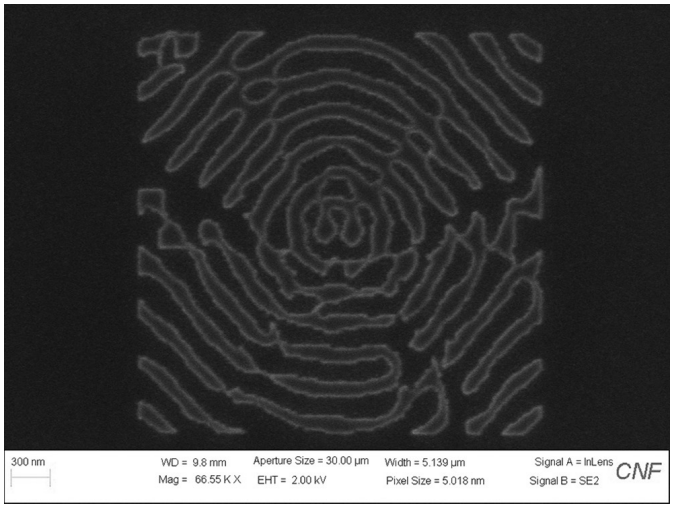

Figure 2: SEM image of the pattern after Cr etch.

Acknowledgements:

We would like to thank the Prof. Alejandro Rodriguez's group for the discussion on and their design of the nanophotonic cavity structure.

References:

[1] Aharonovich, I., Englund, D., and Toth, M. Solid-state single-photon emitters. Nature Photonics 10, 631-641 (2016).

[2] Jungwirth, N. R., and Fuchs, G. D. Optical Absorption and Emission Mechanisms of Single Defects in Hexagonal Boron Nitride. Phys. Rev. Lett. 119, 057401 (2017).

[3] Bennett, C. H., and Brassard, G. Quantum cryptography: Public key distribution and coin tossing. Theoretical Computer Science 560, 7-11 (2014).

[4] Molesky, S., et al. Inverse design in nanophotonics. Nature Photonics 12, 659-670 (2018).

Ultrafast Energy-Efficient Spin-Torque Magnetic Random Access Memories

CNF Project Number: 2444-16

Principal Investigator(s): Robert A. Buhrman

User(s): Lijun Zhu

Affiliation(s): School of Applied and Engineering Physics, Cornell University

Primary Source(s) of Research Funding: Office of Naval Research

Contact: rab8@cornell.edu, lz442@cornell.edu

Primary CNF Tools Used: ASML stepper, Veeco Icon AFM, JEOL JBX-6300FS, AJA sputter

Abstract:

Spin-orbit torques [1-5] have been a hot topic in the research and technology communities due to their great promise for magnetic memories, oscillators and logic of post-Moore era. Here we demonstrate ultrafast energy-efficient magnetic random access memories (MRAMs) [6,7] fabricated at the Cornell NanoScale Science and Technology Facility.

Summary of Research:

We fabricated the spin-torque MRAM devices shown in Figure 1(a). The magnetic multilayer samples are patterned into three-terminal MRAM devices with a three-step procedure. First, we defined the spin Hall channel using DUV lithography (ASML stepper) and ion beam etching and measured the channel size by atomic force microscopy (Veeco Icon). We then defined the elliptical magnetic tunnel junction nanopillars with different aspect ratios and micron-size "via" pillars (as vertical connector between the bottom channel to top contact) onto the spin Hall channel with e-beam lithography (JEOL JBX-6300FS) and ion beam etching, and isolated the pillars with 80 nm thick SiO_2 deposited by an e-beam evaporator. Finally, contacts of Ti/Pt were deposited on the top of the magnetic tunnel junction pillars and "via" pillars for electrical measurements by combining the DUV lithography (ASML stepper), AJA sputtering, and liftoff processes.

Figure 1(b) shows ultrafast, reliable, and efficient current switching of our spin-torque MRAMs.

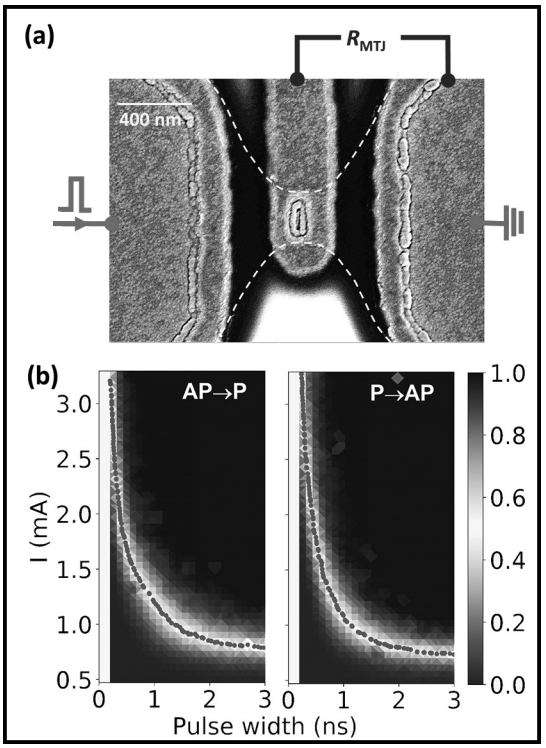

Figure 1: (a) Top-view scanning electron microscopy image of a spin-torque MRAM device; (b) Current-induced switching of the MRAMs. (See pages vi-vii for full color version.)

References:

[1] L. Zhu, D.C. Ralph, R.A. Buhrman, Phys. Rev. Lett. 122, 077201 (2019).

[2] L. Zhu, K Sobotkiewich, X. Ma, X. Li, D.C. Ralph, R.A. Buhrman, Adv. Funct. Mater. 29, 1805822 (2019).

[3] L. Zhu, D.C. Ralph, R.A. Buhrman, Phys. Rev. B 99, 180404 (R)(2019).

[4] L. J. Zhu, D.C. Ralph, R.A. Buhrman, Phys. Rev. B 98, 134406 (2018).

[5] L. Zhu, D.C. Ralph, R.A. Buhrman, Phys. Rev. Appl. 10, 031001 (2018).

[6] L. Zhu, L. Zhu, S. Shi, M. Sui, D. C. Ralph, R. A. Buhrman, Phys. Rev. Appl. 11, 061004 (2019).

[7] L. Zhu, L. Zhu, S. Shi, D. C. Ralph, R. A. Buhrman, Adv. Electron. Mater. 6, 1901131 (2020).

Magnetic Imaging of Ionic Liquid Gated Transition Metal Dichalcogenides

CNF Project Number: 2514-16
Principal Investigator(s): Katja Nowack
User(s): Alexander Jarjour

Affiliation(s): LASSP, Cornell University
Primary Source(s) of Research Funding: Cornell Center for Materials Research (NSF MRSEC, DMR-1719875)
Contact: kcn34@cornell.edu, abj46@cornell.edu
Primary CNF Tools Used: SC4500 evaporators, JEOL 6300, Oxford PlasmaLab 80+ RIE

Abstract:

We report fabrication of superconducting ionic-liquid (IL) gated MoS_2 devices compatible with scanned probe microscopy (SPM). Using a spin-coated IL gate, the thickness of the ionic layer is reduced to less than 0.5 micron, enabling local magnetic measurements of the superconducting state.

Summary of Research:

Atomically thin exfoliated MoS_2 devices have been reported to superconduct at an n-type charge carrier density of $\sim 10^{14}$ cm^{-2} [1] with a critical temperature of approximately $\sim$ 2 K in a monolayer [2]. To achieve the high charge carrier density ionic gating has been employed in the literature, however, this prevents scanned probe measurements due to the macroscopic thickness of the ionic gate on top of the device. Our group is interested in imaging the magnetic response of the superconducting state, using scanning Superconducting QUantum Interference Device (SQUID) microscopy. This technique can be used to measure the superfluid density of a superconductor as a function of temperature, which can reveal information about the order parameter [3].

Our device fabrication is performed in the CNF. First, optical contact lithography is used to pattern liftoff resist for bond pads, long leads from the device area to the bond pads, and a large gate for biasing the ionic liquid. A completed device is shown in Figure 1, which includes these features. The SC4500 electron beam evaporator is then used to deposit a Ti/Pt/Au trilayer. The gold is wet etched in the gate region, exposing the platinum. Thus, the device side of the electrolytic capacitor is gold, and the gate side is platinum, with the aim of minimizing electrochemistry during gating. Using the polymer stamp transfer techniques developed for graphene heterostructures [4], MoS_2 flakes are transferred onto these prepatterned substrates, and any polymer residue is removed by a chloroform dip. Then, contacts are patterned to the flake using the JEOL 6300 electron-beam lithography system, connecting it to the long leads and bond pads. These contacts are then metalized in the SC4500 with Ti/Au. Next, a hall bar geometry is defined with the JEOL 6300, and the Oxford 80 is used to etch the MoS_2. Finally, a vacuum bake is used to remove any residue from the devices. A completed MoS_2 device before liquid gating is shown in the left in Figure 2.

In our lab, an ionic gel is prepared from diethylmethyl(2-methoxyethyl)ammonium bis(trifluoromethylsulfonyl) imide (DEME-TFSI) and polystyrene-poly(methyl methacrylate)-polystyrene (PS-PMMA-PS). In an inert atmosphere, this gel is spin-coated onto the devices, covering the MoS_2 flake and the platinum gate. The device is then transferred into a scanning SQUID microscope and is dessicated under high vacuum for 24 hours before cooldown. Upon cooling to < 10 Kelvin, a superconducting transition is observed. We have measured both DC magnetization and AC magnetic susceptibility of these devices, a first in a van der Waals superconductor. On the right in Figure 2, the AC susceptibility of a device is shown. Positive signals correspond to diamagnetism. The white dashed outline is the device geometry.

Magnetic measurements of the superconducting state are still a work in progress. Magnetic features suggestive of vortex-vortex interactions, including a Berezinskii-Kosterlitz-Thouless transition, are observed but not shown. We continue to improve and refine these measurements and their analysis.

References:

[1] J. T. Ye, et al., Science 338, 1193 (2012).

[2] D. Costanzo, et al., Nature Nanotechnology 11, 339 (2016).

[3] J.A. Bert, et al., PRB Vol 86 (2012).

[4] P. J. Zomer, et al., Appl. Phys. Lett. 105, 013101 (2014).

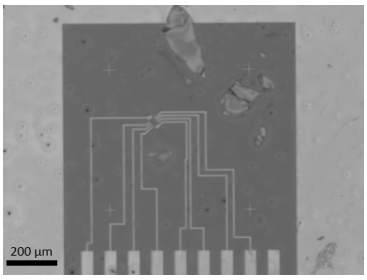

Figure 1: Spin-coated 380 nm ionic gel on MoS_2 few-layer device. Large surrounding metallic region is Pt gate, bars at bottom of image are optically patterned leads to bond pads.

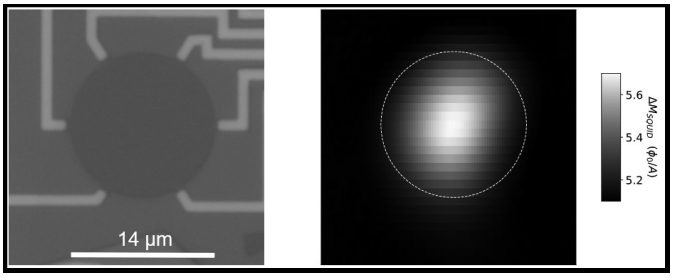

Figure 2: Left, optical image of few layer MoS_2 device fabricated by the authors. Right, magnetic susceptibility map of the same device, as acquired by scanning SQUID microscope.

Two-Dimensional Magnetic Nanoelectromechanical Resonators

CNF Project Number: 2633-18

Principal Investigator(s): Jie Shan, Kin Fai Mak

User(s): Shengwei Jiang

Affiliation(s): Laboratory of Atomic and Solid State Physics, School of Applied and Engineering Physics; Cornell University

Primary Source(s) of Research Funding: Air Force Office of Scientific Research

Contact: jie.shan@cornell.edu, kinfai.mak@cornell.edu, sj538@cornell.edu

Primary CNF Tools Used: Autostep i-line stepper, Hamatech wafer processor develop, Heidelberg mask writer - DWL2000, photolithography spinners, SC4500 odd/even-hour evaporator, DISCO dicing saw

Abstract:

Two-dimensional (2D) layered materials possess out-standing mechanical, electronic and optical properties, making them ideal materials for nanoelectromechanical applications. The recent discovery of 2D magnetic materials has promised a new class of magnetically active nanoelectromechanical systems. In this project, we demonstrate resonators made of 2D magnet CrI_3, whose mechanical resonances depend on the magnetic state of the material.

Summary of Research:

Two-dimensional (2D) layered magnetic materials are attractive building blocks for nanoelectromechanical systems (NEMS): while they share high stiffness and strength and low mass with other 2D materials, they are magnetically active [1-3]. In this project, we develop magnetic NEMS resonators made of 2D chromium triiodide (CrI_3) and investigate the magnetostriction effects in the material.

Figure 1 shows the schematics of the drumhead device structure and the measurement system. The device is made of a bilayer CrI_3 membrane (an antiferromagnet) encapsulated by few-layer graphene and monolayer tungsten diselenide (WSe_2). The few-layer graphene acts as a conducting electrode, and monolayer WSe_2, as a strain gauge [4]. The heterostructure is suspended over a microtrench to form a mechanical resonator.

Figure 2 is an optical image of a typical device. The circular microtrenches of 2-3 μm in radius and 600 nm in depth are patterned on Si/SiO_2 substrates by the combined UV photolithography and plasma etching of the SiO_2 layer. The Ti/Au electrodes are patterned on the Si/SiO_2 substrates by photolithography and metal evaporation. Atomically thin samples of CrI_3, WSe_2, and graphene are first exfoliated from their bulk crystals onto silicon substrates covered with a 300 nm thermal oxide layer. Selected thin flakes of appropriate thickness and geometry are then picked up one-by-one by a stamp consisting of a thin layer of polycarbonate on polydimethylsiloxane (PDMS). The complete heterostructure is first released onto a new PDMS substrate so that the residual PC film on the sample can be

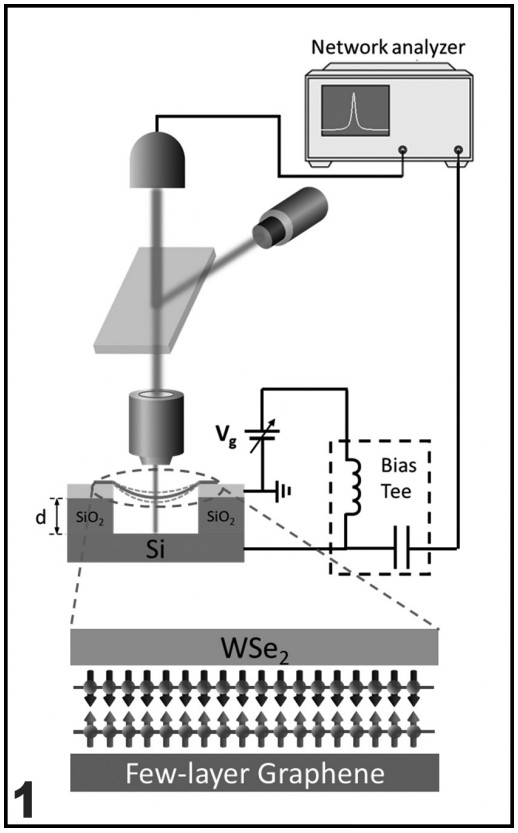

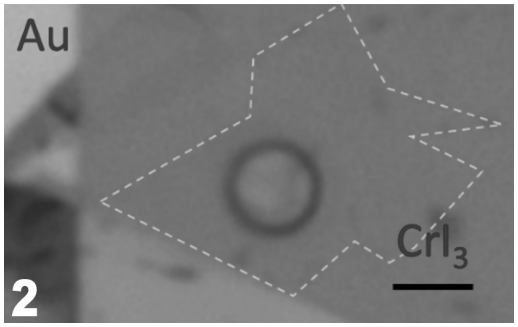

Figure 1, top: *Schematic of the device structure and the measurement system. Filled spheres and arrows denote Cr atoms and spins in the top and bottom CrI_3 layer.*
Figure 2, bottom: *Optical microscope image of a bilayer CrI_3 device suspended over a circular trench. Dashed line shows the boundary of the CrI_3 flake. Scale bar is 4 μm.*

removed. The sample is then deposited onto the substrates with pre-patterned microtrench and Au electrodes.

The resonator is actuated by an R.F. voltage from a vector network analyzer (VNA) through a bias tee (Figure 1). A DC voltage V_g can be superimposed to apply static tension to the membrane. The motion is detected interferometrically by a HeNe laser, which is focused onto the center of the resonator. Figure 3 shows the fundamental resonance mode of a bilayer CrI_3 membrane at V_g = 0. It has a Lorentzian lineshape (solid line) with a peak frequency f around 25.5 MHz and a width around 10 kHz, corresponding to a quality factor of about 2500. The resonance frequency is well described by the continuum model (assuming zero bending stiffness) with fully clamped boundary [5]. It is inversely proportional to the drumhead radius, and is determined by the initial stress on the membrane and the 2D mass density of the membrane.

We investigate the effect of magnetic field on CrI_3 resonators. The nanomechanical resonance of the bilayer CrI_3 device is measured while the out-of-plane field is swept from 1 T to -1 T back to 1 T. The resonance frequency *f* is independent of field except an abrupt redshift of ~ 0.06% when the field magnitude exceeds ~ 0.5 T. We correlate the field dependence of *f* with the sample's magnetic circular dichroism. The latter shows that bilayer CrI_3 is antiferromagnetic (AF) under small fields and undergoes a first-order spin-flip transition around ± 0.5 T to become ferromagnetic (FM) [6]. The mechanical resonance frequency is thus correlated with the sample's magnetic state with the resonance frequency in the AF state larger than in the FM state. This phenomenon can be understood as exchange magnetostriction. We extract the intrinsic saturation magnetostriction in bilayer CrI_3 (10^{-5}), which is comparable to that of elemental ferromagnetic metals.

In conclusion, we have demonstrated a new type of magnetostrictive NEMS based on 2D CrI_3. Our results also establish the basis for mechanical detection of the magnetic states and magnetic phase transitions in 2D layered magnetic materials.

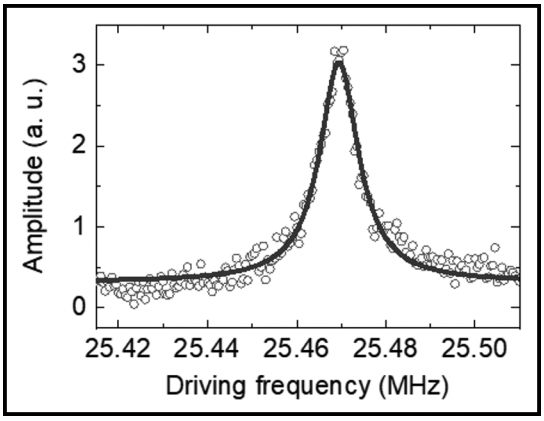

Figure 3: Fundamental mechanical resonance (symbols) of a bilayer CrI_3 resonator (radius 2 μm) and a Lorentzian fit of the resonance spectrum (solid line).

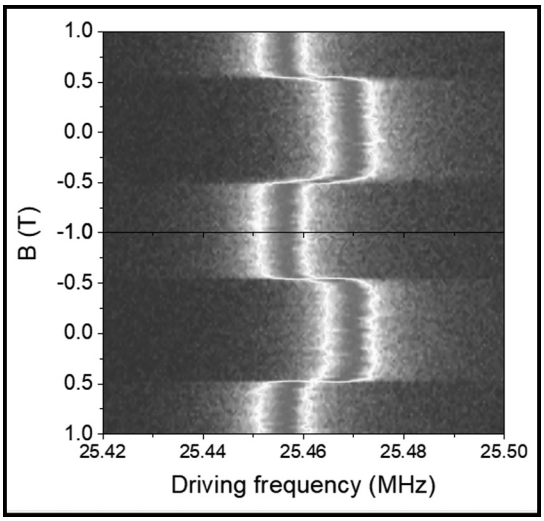

Figure 4: Normalized vibration amplitude of a bilayer CrI_3 resonator vs. driving frequency under an out of-plane magnetic field that sweeps from 1 T to -1 T to 1 T.

References:

[1] Craighead, H. G. Nanoelectromechanical Systems. Science 290, 1532-1535 (2000).

[2] Huang, B., et al. Nature 546, 270 (2017).

[3] Gong, C., et al. Nature 546, 265-269 (2017).

[4] Frisenda, R., et al. Biaxial strain tuning of the optical properties of single-layer transition metal dichalcogenides. npj 2D Mater. Appl. 1, 10 (2017).

[5] Bunch, J. S., et al. Electromechanical Resonators from Graphene Sheets. Science 315, 490-493 (2007).

[6] Jiang, S., Shan, J., and Mak, K. F. Nature Materials 17, 406 (2018).

Mass Transport on Graphene

CNF Project Number: 2767-19

Principal Investigator(s): Scott Schiffres

User(s): Yingchun Jiang, Morteza Bagheri

Affiliation(s): Mechanical Engineering, Binghamton University

Primary Source(s) of Research Funding: Startup funding

Contact: sschiffr@binghamton.edu, yjiang89@binghamton.edu, mortezahb@binghamton.edu

Primary CNF Tools Used: Heidelberg DWL2000, ABM, MA6 contact aligner, Oxford 81 etcher, YES Asher, SC4500 evaporator, Zeiss Ultra SEM

Abstract:

A graphene channel with various widths for atomic mass transportation was fabricated photolithographically. Transportation of aluminum nanoparticles on graphene ribbon under ambient condition was demonstrated.

Summary of Research:

The development of nanotechnology requires versatile manipulation tools for atomic scale assembly and controlled material delivery. Scanning tunneling microscope (STM), atomic force microscope (AFM) have been demonstrated as powerful tools for manipulation of atoms and molecules on clean surfaces. However, these tools suffer from low delivery efficiency: they are not capable to deliver nanometer scale features containing large amounts of atoms, and they cannot deliver atom efficiently to the desired work area (sticky). Carbon nanotubes and graphene have been suggested as possible nanoscale mass conveyors with an electric field as the source of applied force. Controllable and reversible atomic metal transportation along carbon nanotubes (CNTs) and transport of more than 10^7 atoms have been demonstrated [1-3]. Graphene is mechanically robust and chemically inert; it can sustain large current density similar to CNTs. It has the advantage over CNTs that more complicated mass transport circuits can be designed with lithographic techniques [4-7].

We fabricated graphene ribbon with traditional photolithography process as shown in Figure 1. Pt/Au contact pads were patterned on top of the graphene channel or the graphene electrodes. Thin Al pads (around 2 μm wide and 7 nm thick) were evaporated on the graphene circuits (as shown in Figure 2 (a)) for demonstration of atomic mass transportation on graphene. After deposition of the Al pads, it was annealed under vacuum to reflow the Al, the topography of the Al after annealing is shown in Figure 3 (b). The Al atoms are manipulated by applying large electric field along the graphene circuit. Mass loss of Al and mass increase near the electrode were observed after applying large electric field, as shown in Figure 3.

Conclusions and Future Steps:

The motion of thin Al pads along graphene circuit under ambient condition was demonstrated. The characterization of the actuation should be studied further, especially the contribution of the thermal effect to the motion. We should also find the electric field that is large enough for continuous manipulation of the atoms without damaging the graphene device.

References:

[1] B.C. Regan, S. Aloni, R.O. Ritchie, U. Dahmen, A. Zetti, Carbon nanotubes as nanoscale mass conveyors, Nature. 428 (2004) 924-927. doi:10.1038/nature02496.

[2] Z. Ren, Y. Lan, Y. Wang, Subnanometer motion of cargoes driven by thermal gradients along carbon nanotubes, Science (80-.). (2012) 7-43. doi:10.1007/978-3-642-30490-3_2.

[3] N. Mingo, L. Yang, J. Han, Current-induced forces upon atoms adsorbed on conducting carbon nanotubes, J. Phys. Chem. B. 105 (2001) 11142-11147. doi:10.1021/jp011491s.

[4] S. Hertel, F. Kisslinger, J. Jobst, D. Waldmann, M. Krieger, H.B. Weber, Current annealing and electrical breakdown of epitaxial graphene, Appl. Phys. Lett. 98 (2011) 2009-2012. doi:10.1063/1.3592841.

[5] A. Barreiro, R. Rurali, E.R. Hernández, A. Bachtold, Structured graphene devices for mass transport, Small. 7 (2011) 775-780. doi:10.1002/smll.201001916.

[6] J. Moser, A. Barreiro, A. Bachtold, Current-induced cleaning of graphene, Appl. Phys. Lett. 91 (2007) 1-4. doi:10.1063/1.2789673.

[7] D. Solenov, K.A. Velizhanin, Adsorbate transport on graphene by electromigration, Phys. Rev. Lett. 109 (2012) 1-5. doi:10.1103/PhysRevLett.109.095504.

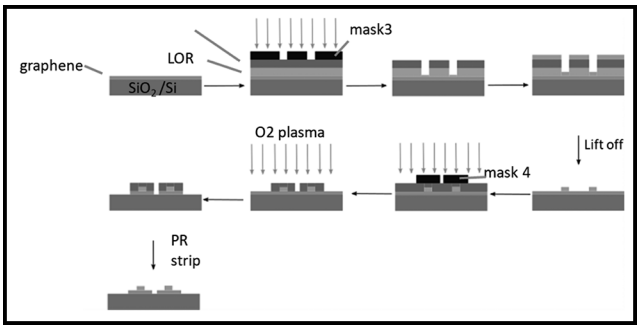

Figure 1: Process flow for making Al pads on graphene ribbon by lift off.

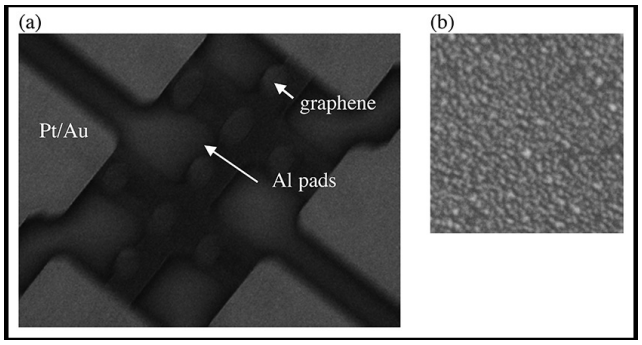

Figure 2: (a) SEM image of the graphene circuit with Al pads.
(b) Topography of thin aluminum film after annealing.

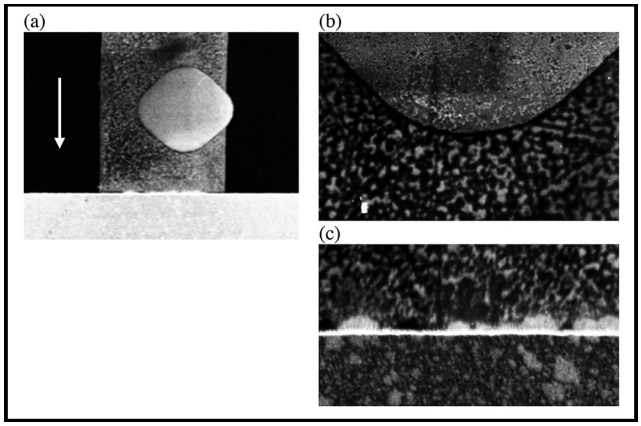

Figure 3: (a) SEM image of an Al pad after applying electric field in air.
(b) Edge of the Al showing mass loss after applying electric field.
(c) edge of the electrodes showing mass increase.

Superconducting Thin Film Growth, Post-Treatments, and Defects Investigation

CNF Project Number: 2779-19

Principal Investigator(s): Matthias Liepe

User(s): Zeming Sun

Affiliation(s): Cornell Laboratory for Accelerator-based Sciences and Education, Cornell University

Primary Source(s) of Research Funding: National Science Foundation under Grant No. PHY-1549132

Contact: MUL2@cornell.edu, zs253@cornell.edu

Website: https://physics.cornell.edu/matthias-liepe

Primary CNF Tools Used: Chemical vapor deposition system, Oxford FlexAL ALD, Arradiance Gemstar-6 atomic layer deposition system, Thermal/ E-gun evaporation system, Woollam spectroscopic ellipsometer, Zygo optical profilometer, P10 profilometer

Abstract:

Superconducting radio frequency (SRF) cavities are important in accelerating charged particle beams that have broad applications such as colliders, neutron sources, and light sources. Niobium tin (Nb_3Sn), vanadium silicate (V_3Si), and magnesium diboride (MgB_2) are the most promising superconductor candidates for the next generation SRF cavities. However, their thin film growth is still challenging due to surface roughness, defect generation, grain boundaries, and surface oxidation. Thus, this project investigates the growth mechanisms of superconducting films deposited via electroplating, sputtering, chemical vapor deposition approaches, and explores post-processing techniques, such as electropolishing, surface passivation, and laser annealing, to mitigate the crystal defects, surface roughness, and oxidation. Moreover, this project studies the impact of defects on the SRF performance through studying the performance of artificial structures that are fabricated at the Cornell NanoScale Science and Technology Facility (CNF).

Summary of Research:

(1) We demonstrated ultra-low surface roughness Nb_3Sn superconductors (detailed in Reference [1]). This is achieved by thermal conversion of a pre-deposited Sn film that is uniform, smooth, dendrite-free, and has strong adhesion. Electroplating, as an excellent method for coating intricate SRF cavity surface, is used to enable the deposition process of a high-quality Sn film. The resultant Nb_3Sn shows an extremely low surface roughness of 65 nm as shown in the atomic force microscopy image (Figure 1).

(2) Alternative deposition approaches such as sputtering, chemical vapor deposition, and chemical methods are explored to deposit Nb_3Sn and V_3Si. For example, a fast-ion transport reaction is demonstrated for generating Nb_xSn (detailed in Reference [2]). X-ray photoelectron spectroscopy (XPS) depth profiling provides direct evidence of film stoichiometry (Figure 2). Another success is sputtering of Nb_3Sn and V_3Si have been enabled on Nb and Cu substrates (Figure 3). The optimization of film quality is ongoing.

(3) Post treatments such as electropolishing and laser annealing are explored to improve the superconductor film quality. For example, the chemical vapor deposited Nb film is greatly smoothed via electropolishing with the surface roughness reduced by half (detailed in Reference [3]). Moreover, the laser annealing technique has been studied to reduce film surface roughness. A titanium nitride film was deposited via atomic layer deposition to improve the laser light absorption. The deposition condition is optimized for desired film thickness and refractive index (Figure 4). With this critical absorption layer, the laser is able to melt the Nb_3Sn surface and remove the sharp surface pits.

(4) MgB_2 superconducting thin film is easily oxidized in air which hinders its wider application. An aluminum nitride film is deposited on the film using plasma-enhanced atomic layer deposition to passivate the surface. The interface is being analyzed using XPS.

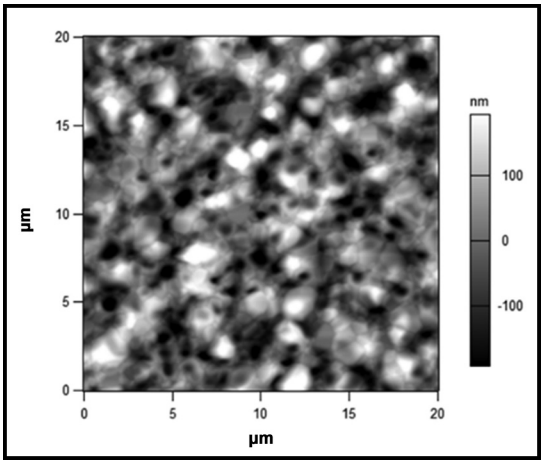

Figure 1: Atomic force microscopy of thermally converted Nb_3Sn from electroplated Sn films, showing an extreme low surface roughness.

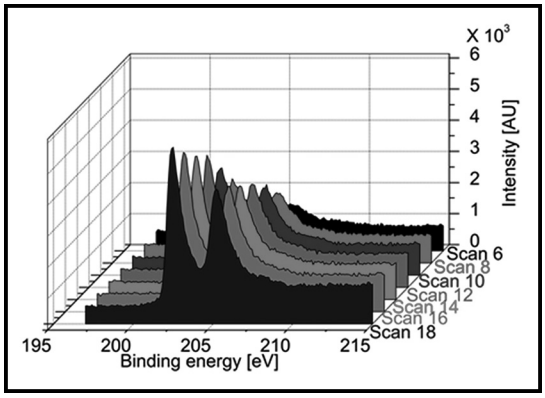

Figure 2: X-ray photoelectron spectroscopy depth profiling of fast-transported Nb_xSn film showing Nb 3d intensity approaching stoichiometry of Nb_3Sn.

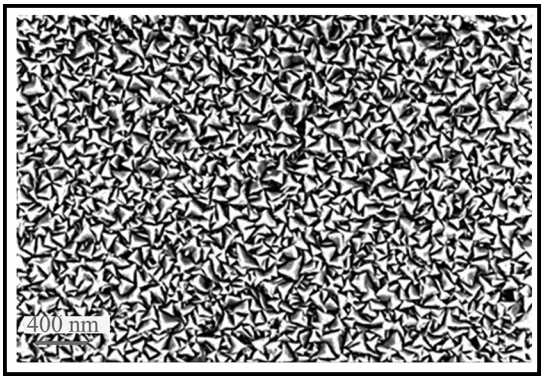

Figure 3: SEM of the sputtered Nb_3Sn films.

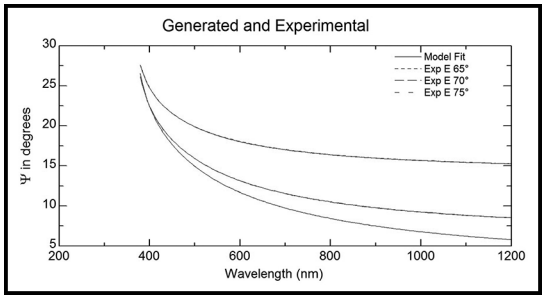

Figure 4: Ellipsometry modeling for optimizing titanium nitride deposition by thermal atomic layer deposition.

References:

[1] Z. Sun, M. Liepe, T. Oseroff, R.D. Porter, T. Arias, N. Sitaraman, A. Connolly, J. Scholtz, M.O. Thompson, Electroplating of Sn film on Nb substrate for generating Nb-Sn thin films and post laser annealing, Proceeding of SRF'19, Dresden, Germany, 2019.

[2] Z. Sun, M. Liepe, J.T. Maniscalco, T. Oseroff, R.D. Porter, D. Zhang, X. Deng, Fast Sn-ion transport on Nb surface for generating NbxSn, Proceeding of NAPAC'19, Michigan, 2019.

[3] Z. Sun, M. Ge, K. Howard, M. Liepe, J. Maniscalco, T. Oseroff, R. Porter, V. Arrieta, S. McNeal, TESLA Technology Collaboration workshop, Geneva, Switzerland, February, 2020.

Development of Strain-Tunable Bilayer Graphene Devices

CNF Project Number: 2790-19

Principal Investigator(s): Katja C. Nowack

User(s): Brian T. Schaefer, Justin Oh

Affiliation(s): Laboratory of Atomic and Solid-State Physics, Department of Physics; Cornell University

Primary Source(s) of Research Funding: Cornell Center for Materials Research with funding from the NSF MRSEC program (DMR-1719875), National Science Foundation Graduate Research Fellowship under Grant No. DGE-1650441

Contact: kcn34@cornell.edu, bts72@cornell.edu

Website: http://nowack.lassp.cornell.edu/

Primary CNF Tools Used: Zeiss Supra SEM/Nabity, Trion Minilock III ICP etcher, 5x stepper

Abstract:

The direct application of uniaxial strain is a versatile and low-disorder technique to tune the electronic properties of materials [1]. Specifically, in two-dimensional materials with a hexagonal lattice, strain can result in a net magnetization with a purely orbital origin [2]. Dual-gated bilayer graphene is a versatile platform for studying this magnetization because the electronic bandgap and charge carrier density can be tuned widely and independently [3]. Here, we describe our efforts towards fabricating strainable multi-terminal bilayer graphene devices on flexible polyimide substrates. We continuously apply strain up to ~ 1.4% confirmed using Raman spectroscopy.

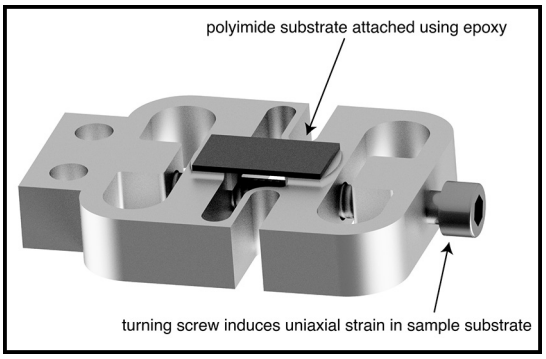

Figure 1: Custom titanium-based strain apparatus4 with polyimide substrate attached using Stycast 2850FT epoxy.

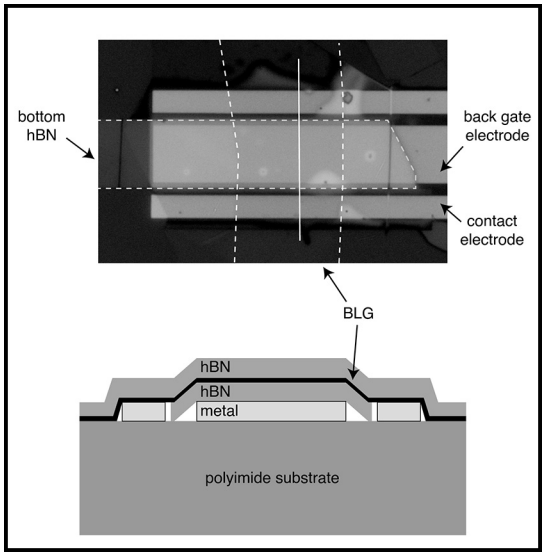

Figure 2: Top: optical image of a bilayer graphene device fabricated upon a polyimide substrate. Bottom: cross-sectional schematic along the solid line in the optical image.

Summary of Research:

We use the custom titanium-based apparatus [4] illustrated in Figure 1 to apply strain to a polyimide substrate upon which our bilayer graphene devices are fabricated. Turning the screw displaces the two halves of the apparatus and enables continuous application of uniaxial tensile strain to a sample mounted to the split central platform. The maximum strain depends on the elastic modulus and geometry of the sample along with the yield strength of the epoxy used to attach the sample. Optical images of lithographically defined features on the surface of the substrate suggest a typical maximum strain of ~ 2% for polyimide substrates limited by failure of the epoxy.

Figure 2 shows an optical image and cross-sectional schematic of a strainable bilayer graphene device. We initially pattern metal electrodes for the device back gate and contacts onto a bare polyimide substrate. Next, we use a polymer-stamp-based dry-transfer technique [5] to sequentially pick up and transfer exfoliated flakes of bilayer graphene (BLG) and hexagonal boron nitride (hBN) onto the pre-patterned metal features.

We first transfer a single hBN flake onto the patterned electrodes and use reactive-ion etching (Trion Minilock III ICP Etcher) to uncover the metal contact electrodes. On top of this, we transfer a stack of hBN/BLG to complete the device. The top hBN flake facilitates the transfer of BLG, while the bottom hBN flake is a dielectric for the back gate. Encapsulation with hBN on both top and bottom improves the electronic quality of graphene devices [5]. Previous iterations of the fabrication process suggest that the direct areal contact between the BLG flake and polyimide substrate in our current design is essential for effective strain transfer from the substrate to the BLG flake.

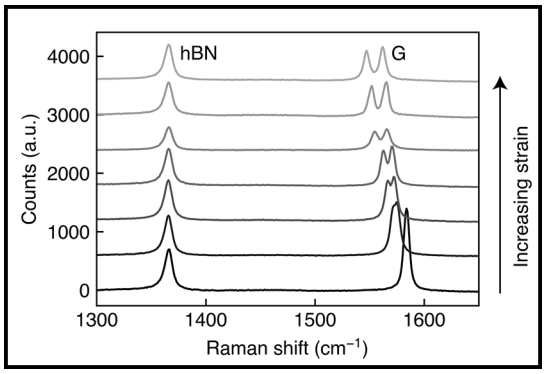

Figure 3: Strain evolution of the in-plane Raman peaks for BLG (labeled "G") and hBN.

We use Raman spectroscopy to monitor changes in the vibrational modes of the lattice under application of strain, and use the position of the BLG "G" peak to estimate the amount of strain transfer. Figure 3 shows the evolution of the in-plane Raman peaks for hBN ("hBN", ~ 1366 cm^{-1} at zero strain) and BLG ("G", ~ 1583 cm^{-1} at zero strain) upon straining the substrate. The G peak shifts to lower wavenumber and splits into two distinct peaks, as expected for a hexagonal lattice with rotational symmetry broken by in-plane uniaxial strain [6]. The hBN peak is also expected to shift under uniaxial strain, so the unchanging peak position suggests that strain is not transferred to hBN. The hBN-graphene interface exhibits notably low friction [7], so the lack of strain in the hBN layer is not surprising. Comparing the peak positions to those reported in the literature [6], we estimate that we induced at most ~ 1.4% uniaxial strain into this BLG device.

Conclusions and Future Steps:

We demonstrate application of uniaxial strain in a two-terminal bilayer graphene device fabricated on a metallic back gate and polyimide substrate. Moving forward, we aim to add a top gate electrode and identify improvements to the process that increase the yield of devices that strain reliably. This motivates investigation of the mechanism of strain transfer from the substrate into BLG. We then will study the effects of strain on the magnetic properties of our devices and extend this technique to other two-dimensional material systems.

References:

[1] Wang, L. et al. Mobility Enhancement in Graphene by *in situ* Reduction of Random Strain Fluctuations. Phys. Rev. Lett. 124, 157701 (2020).

[2] Lee, J., Wang, Z., Xie, H., Mak, K. F., and Shan, J. Valley magnetoelectricity in single-layer MoS_2. Nat. Mater. 16, 887-891 (2017).

[3] Zhang, Y., et al. Direct observation of a widely tunable bandgap in bilayer graphene. Nature 459, 820-823 (2009).

[4] Sunko, V., et al. Direct Observation of a Uniaxial Stress-driven Lifshitz Transition in Sr_2RuO_4. npj Quantum Materials 4 (2019).

[5] Wang, L., et al. One-dimensional electrical contact to a two-dimensional material. Science 342, 614-617 (2013).

[6] Tsoukleri, G., Parthenios, J., Galiotis, C., and Papagelis, K. Embedded trilayer graphene flakes under tensile and compressive loading. 2D Mater. 2, 024009 (2015).

[7] Song, Y., et al. Robust microscale superlubricity in graphite/hexagonal boron nitride layered heterojunctions. Nat. Mater. 17, 894-899 (2018).